Cryo-ET of infected cells reveals that a succession of two lattices drives vaccinia virus assembly

Miguel Hernandez-Gonzalez[1], Thomas Calcraft[2], Andrea Nans[3], Peter B Rosenthal[2] and Michael Way[1, 4] *

[1]Cellular signalling and cytoskeletal function laboratory, The Francis Crick Institute, 1 Midland Road, London, NW1 1AT, UK

[2]Structural Biology of Cells and Viruses Laboratory, The Francis Crick Institute.

[3]Structural Biology Science Technology Platform, The Francis Crick Institute.

[4] Department of Infectious Disease, Imperial College, London W2 1PG, UK

*To whom correspondence should be addressed. Email: michael.way@crick.ac.uk

Running title: Cryo-ET of vaccinia infected cells

Abstract

During replication, vaccinia virus and other poxviruses such as monkeypox first assemble non-infectious spherical immature virions (IV) in the cytoplasm of infected cells. The IV membrane, which is fully coated by a viral D13 lattice, encapsidates both viral proteins and the DNA genome. Subsequently, the D13 lattice is lost and IV transitions into the brick-shaped intracellular mature virus (IMV) with an organised core enclosing the genome. We have an overview of the maturation of IV into IMV but our structural understanding remains limited. Here, we performed cryo-electron tomography of frozen-hydrated vaccinia-infected cells to structurally characterise the maturation process in situ. We found that D13-coated IV have similar diameters and lattice dimensions to spherical D13 assemblies formed in vitro, confirming the size of IV is determined by D13. During IMV formation a new pseudohexagonal lattice forms inside IV to produce the viral core. This lattice is composed of trimeric pillars with outward projections that appears as a palisade in cross-section. Strikingly, the diameter of IV precisely matches the IMV long axis, suggesting the length of the core, and hence the IMV, is determined by the D13 lattice. During maturation the viral membrane becomes corrugated as it adapts to the shape of the core. This suggests that the 50% reduction in volume during the transition of IV to IMV does not require membrane removal. Our observations suggest that the consecutive D13 and palisade lattices structurally define vaccinia assembly and maturation.

Significance statement

Poxviruses such as variola virus (smallpox) and monkeypox induce disease in humans. Other poxviruses, including vaccinia virus and modified vaccinia Ankara (MVA), are used as vaccine vectors. Despite their importance, a structural understanding of how infectious poxvirus virions assemble in the cytoplasm of infected cells is lacking. In this study, we used cryo-electron tomography of frozen-hydrated vaccinia infected cells to structurally characterise the maturation of spherical immature virions into the infectious brick-shaped intracellular mature virus. These high-resolution in situ observations reveal new features concerning the viral membrane and the inner core of mature virions. The model that emerges suggests that two consecutive viral-derived protein lattices drive vaccinia assembly and maturation.

Introduction

Poxviruses are large double stranded DNA viruses that replicate and assemble their virions in cytoplasmic perinuclear viral factories (1). The family includes variola virus, the causative agent of smallpox, and monkeypox as well as vaccinia, the most studied family member which was used as the vaccine to eradicate smallpox (2, 3). During its replication cycle, vaccinia initially assembles into infectious intracellular mature virions (IMV), which are released when infected cells lyse (4). Prior to cell lysis, however, some IMV become enveloped by a Golgi cisterna or endosomal compartment to form intracellular enveloped virions (IEV) (5-7) (Figure 1A). IEV undergo kinesin-1 mediated microtubule transport to the plasma membrane, where they fuse to release extracellular enveloped virions (EEV) that promote the long-range spread of infection (8, 9). Alternatively, after fusion some virions (cell-associated enveloped virus, CEV) remain attached to the cell to stimulate actin-dependent cell-to-cell spread of the virus (10-13).

The first step in the spread of vaccinia infection is the assembly of IMV, which are the precusor to all subsequent forms (IEV, EEV and CEV) of the virus. IMV formation is initiated when endoplasmic reticulum (ER) associated viral membrane assembly proteins (VMAPs) promote the formation of isolated membrane crescents in the cytoplasm of infected cells (14-16). The characteristic shape of the crescents is determined and maintained by the D13 scaffolding viral protein, which forms trimers that assemble into a hexameric lattice coating the outer surface of the membrane (14, 15, 17, 18). In vitro structural analysis of recombinant D13 reveals it has a double-jelly-roll structure composed of 8 antiparallel ß-strands that self assembles into a honeycomb lattice of pseudo-hexagonal trimers (19-22). Ultimately, membrane crescents develop into spherical immature virions (IV) which encapsidate the viral genome and proteins required to produce an IMV (15, 17, 18, 23). In a process that is still not understood but involves the proteolytic cleavage of viral proteins and the formation of disulphide bonds, spherical IV undergo a dramatic reorganization into brick-shaped IMV (24, 25). During this maturation process, the D13 honeycomb lattice is lost, and a biconcave viral core assembles around the viral genome (23). The outer layer of the viral core forms a paracrystalline palisade-like structure that has been reported to be discontinuous (23, 26, 27). In addition, two dense proteinaceous aggregates, known as the lateral bodies, assemble in the cavity between the outer viral membrane and the biconcave viral core (23, 26, 28).

Vaccinia virion assembly has been extensively studied. Nevertheless, the key structural determinants that govern the changes occurring during the IV to IMV transistion as well as

106 those that define the IMV remain unknown. To obtain detailed ultra-structural insights into
107 this maturation process, we have now performed cryo-electron tomography (cryo-ET) of
108 vaccinia infected cells. Our analysis reveals that a succession of two different viral lattices
109 drives assembly of IMV: D13 shapes the IV membrane, which subsequently coalesces onto
110 the pseudohexagonal palisade lattice, which is reminiscent of a viral capsid.
111
112 **Results**
113 **Electron cryo-tomography of vaccinia virus in infected cells**
114 Cryo-tomograms of thin cellular regions containing IV and IMV were recorded from the
115 periphery of HeLa cells infected with vaccinia virus for 8 hours (Figure 1B, C and S1, Movie
116 1 and 2). IV, fully coated by the viral D13 lattice, are largely spherical and have a diameter
117 of 351.89 ± 2.88 nm (Table S1). Analysis of tomograms in 3D, however, reveals that a
118 proportion of IV despite being closed and fully coated by D13 have a single invagination of
119 the viral membrane (Figure 1B). This suggests that the D13 lattice is flexible and can
120 accommodate both positive and negative curvatures present on virions with invaginations.
121 This D13 lattice flexibility is also evident from its ability to coat the exterior of "open
122 spheres" with different membrane curvature (also known as crescents due to their shape
123 when seen in a middle view) during IV formation (Figure 2A, B and Movie 3).
124
125 The interior of the majority of IV, which contain viral DNA and proteins required for virion
126 assembly, are homogenous and lack any of the distinctive regions or layers seen in IMV
127 (Figure 1B). In a few cases, however, we could observe a single dense striated structure
128 inside IV corresponding to the nucleoid (viral DNA genome) before it decondenses (Figure
129 2C and S2), as seen in previous ultra-structural analysis of thin EM sections of vaccinia
130 infected cells (28). We also found examples of related striated structures in the cytoplasm
131 adjacent to, or in direct association with, assembling IV (Figure 2D, E). Consistent with the
132 interpretation that the example shown in Figure 2E represents the viral genome being
133 inserted into assembling IV, structured illumination microscopy together with deconvolution
134 (125 nm resolution) also reveals the presence of elongated DNA structures associating with
135 virions, identified by RFP-A3, in the viral factory (Figure 2F). Our 3D tomographic
136 observations of assembling IV using cryo-ET were consistent with previous ultra-structural
137 analysis of vaccinia infected cells using electron microscopy (16-18, 29, 30).
138
139 **In situ structure of the hexagonal D13 lattice**
140 Structural analysis of recombinant D13 in isolation has provided a detailed molecular
141 understanding of the D13 trimer (19-22). However, the macromolecular arrangements of

142 the D13 lattice on IV in infected cells have largely been studied by deep-etch EM (17, 18).
143 Given the clear lattices present on the IV surface in our tomograms (Figure 3A, Movie 4), we
144 analysed the structure of the D13 lattice in situ by subtomogram averaging. We obtained
145 maps by averaging surface sectors revealing hexamers of trimer arrangements with a lattice
146 spacing of 133 Å, in agreement with lattices described for in vitro assembled D13 and deep-
147 etch EM honeycombs (Figure 3B). Rigid-body docking of the high-resolution structure of a
148 D13 trimer (PDB: 7VFE) into the map shows the packing of D13 trimers is consistent with
149 that recently reported (19). While at much lower resolution, precluding a detailed
150 description of interface residues, the arrangement of D13 on the spherical IV surface does
151 not appear to include a relative twist of trimeric axes between adjacent trimers as observed
152 in single particle dimers or tubular assembles.
153
154 From the hexagonal packing of D13 in the subtomogram average, we estimate that ~5,300
155 D13 trimers will cover the surface of a spherical IV. The packing density and radius of the
156 D13 lattice on IV are compatible with an icosahedrally symmetric architecture with a
157 triangulation number (T) in the neighborhood of 268. We have not confirmed the presence
158 of icosahedral symmetry, which would require pentameric arrangements of D13 trimers,
159 such as those that have been identified in vitro (19). Finally, we observed a gap of ~5.6 nm
160 between the innermost surface of the D13 lattice and the membrane of the IV. This gap
161 cannot be explained by any unresolved N- or C-terminal residues of D13 and must therefore
162 be bridged by another protein such as A17 (21).
163
164 **Structure of intracellular mature virus in infected cells**
165 The internal organisation, dimensions and shape of IMV, which are "brick-shaped"
166 membrane-bound virions, contrast dramatically with those of IV (Figure 1). Analysis of the
167 size and shape of IMV in 3D reveals they can be approximated to a triaxial ellipsoid of 352 x
168 281 x 198 nm with a calculated volume of 1.02 x 10^7 nm^3 (Figure 4, Table S1 & Movie 5).
169 The outer membrane of IMV has a corrugated appearance and the D13 lattice is absent.
170 There is, however, a new additional outer layer of 6.67 ± 0.11 nm on the viral membrane
171 that was not present on IV (Figure 4). Underneath the viral membrane there is a palisade-
172 looking structure consisting of a series of turret-like densities in cross-section (12.5 nm
173 thick) that is associated with a inner wall that is 3.84 ± 0.09 nm thick (Figure 4A). Depending
174 on the orientation of the virion, the interior organisation of the IMV appears very different.
175 In the mid view of its two widest dimensions (352 x 281 nm), the palisade appears in contact
176 with the viral membrane. However, in the orthogonal lateral view (352 x 198 nm) the
177 palisade structure, which only contacts the viral membrane at the ends of the virion (Figure

178 4B), forms a dumbbell shape that results in the formation of two concavities. Each cavity
179 contains a single dense and amorphous structure corresponding to a lateral body. The space
180 between the viral membrane and the palisade varies between 9.28 ± 0.18 nm and 46.53 ±
181 2.72 nm, the latter being where the lateral bodies are accommodated (see Table S1 for
182 detailed measurements). 3D tomographic analyses reveal that the palisade is a semi-regular
183 array when viewed from above (Figure 4C, D).
184
185 The semi-regular organisation of the palisade is most apparent in naked cores, which lack
186 the viral membrane and are occasionally found in the cytoplasm (Figure 5A, B).
187 Segmentation of our 3D tomograms reveals the palisade is a continuous structure without
188 fenestrations that defines the virus core, including the regions that contact the lateral
189 bodies (Figure 4E, Movie 6). Inside the core, there are no obvious higher order structures.
190 There are, however, interconnected densities that vary between virions but tend to
191 accumulate beneath the inner wall of the core (Figure 4A). These densities are especially
192 apparent in the compressed region underneath the lateral bodies (Figure 4C). Such densities
193 associated with the inner wall of the core potentially represent the viral genome and its
194 associated proteins given its high contrast. Another characteristic that is evident in
195 midplane views of approximately half of the IMV (48.9%, n = 94), is that one corner of the
196 virion (and in a few cases, two corners) appears as a straight or flattened "cut corner"
197 (Figure 1C and Figure S3). This characteristic is intrinsic to the core wall as it is also apparent
198 in naked cores (Figure 5A, Movie 7) and has been previously observed in purified cores (27).
199 In addition, these naked cores lack the two densities corresponding to lateral bodies but
200 have associated spaghetti-like structures contacting the palisade surface (Figure 5A). These
201 flexible polymers, which are 2.6 nm in diameter, form an exclusion zone of ~ 40 nm around
202 the naked core (Figure 5A). Furthermore, it was noticeable that naked cores have randomly
203 distributed ring like structures on their surface that were not observed in IMV. These rings
204 seem to protrude 10-20 nm from the palisade surface and had inner and outer diameters of
205 4.5 ± 0.1 nm and 9.9 ± 0.1 nm, respectively (Figure 5C).
206
207 **The distinct hexagonal core lattice of infectious vaccinia virions**
208 During viral egress, some IMV become triple-membraned intracellular enveloped virions
209 (IEV) after envelopment by a Golgi cisterna or endosomal compartment (Figure 1A).
210 Subsequent fusion of the IEV with the plasma membrane liberates double-membraned
211 extracellular enveloped virions (EEV) that are known as cell-associated extracellular
212 enveloped virions (CEV) if they remain attached to the outside of the cell (7). Our
213 tomograms reveal that the additional membranes acquired by envelopment are not

214 corrugated (Figure 6A). In the case of IEV, the outer membrane is also not always in close
215 contact with the underlying membrane (see Table S1 for virion measurements). The
216 dimensions and structure of the IMV are also unaffected by envelopment (Figure 6A).
217 Notably, the palisade fully coats the viral core in all infectious virions and its organisation
218 appears unaltered (Figure 6A-C). To study the architecture of the palisade, we performed
219 subtomogram averaging separately using IMV, IEV and CEV/EEV particles. Maps obtained
220 from the different virion types, all displayed the same organisation and lattice parameters
221 (P6 symmetry with a=b=89 ± 2 Å, θ=120°) (Fig S4). A new combined map obtained by
222 averaging all particle types, reveals that the palisade is composed of trimeric pillars with
223 projecting lobes that interact with neighbouring pillars with local hexagonal symmetry
224 (Figure 6D). These pillars are embedded in an unfeatured inner wall. While further details
225 are required to understand its molecular composition, this arrangement appears to be
226 flexible enough to assemble a continuous biconcave capsid structure.
227
228 **Maturation of IV to IMV**
229 Radical changes in the organisation, dimensions and shape of IV result in the formation of
230 IMV (Figure 7). Based on our tomograms, IV have an average diameter of 351.89 ± 2.88 nm
231 and a volume of 2.28 x 10^7 nm^3 for completely spherical particles (Figure 7A). In contrast,
232 "brick-shaped" IMV have a volume of 1.02 x 10^7 nm^3 based on dimensions of 352 x 281 x 198
233 nm (Figure 7A). This reduction in volume is accompanied by a dramatic corrugation of the
234 viral membrane, together with the loss of the D13 lattice. To better understand this
235 corrugation process, we measured the middle-plane perimeter of the viral membrane in IV
236 and IMV, following the wrinkles of the viral membrane to obtain its contour length. We
237 found that the membrane contour is virtually identical in IV and IMV, as well as in the
238 equivalent innermost mmembrane of EEV/CEV (~1100 nm, Figure 7B). This suggests the viral
239 membrane folds during maturation, which would explain the reduction in volume without
240 any detectable loss of membrane surface. In addition to reducing their volume by ~50%, IVs
241 also change their shape when they mature into IMV, becoming a triaxial ellipsoid. Strikingly,
242 the longest IMV dimension matches the diameter of IV (Figure 7A, B), suggesting that the
243 major axis of IMV is dictated by the IV diameter. In our tomograms we also found particles
244 that may represent intermediates and/or defective examples of IV maturation. These
245 include examples where the palisade is fully formed but the IV membrane, which either
246 lacks or is partially coated with D13, is not associated with the viral core (Figure 7C). It is
247 also interesting that we did not observe any virions with partially formed cores suggesting
248 that palisade formation is likely to be rapid or occurs en bloc.
249

250 **Discussion**

251 Previous ultra-structural analyses of vaccinia infected cells by electron microscopy over
252 many decades have provided important insights into the assembly of vaccinia virions. These
253 studies, however, have largely been conducted on fixed sections of infected cells which can
254 have fixation, processing and staining artifacts. Cryo-EM studies, analysing viral entry or
255 purified virions, have demonstrated the potential of using cryo-electron microscopy to study
256 vaccinia structure (26, 27, 31, 32). Here, we apply cryo-ET to image the thin edge of plunge-
257 frozen, vaccinia virus-infected cells, revealing virus architecture in situ. While there is
258 confirmation of past work, important new features emerged from our study. We found that
259 during maturation to IMV, spherical IV lose their D13-coat and reduce their volume by ~50%.
260 During this process, the outer viral membrane becomes corrugated when it associates with
261 the capsid-like palisade layer and the lateral bodies. The palisade, which remains unaltered
262 during subsequent virion morphogenesis, is a continuous regular lattice with
263 pseudohexagonal symmetry that fully covers the viral core. Our observations suggest that
264 these two lattices, D13 and the palisade, drive vaccinia assembly and maturation.
265
266 We found that the D13 lattices coating IV have a similar architecture to the D13 lattices
267 formed in vitro (19). Furthermore, Hyun et al. produced D13 spherical IV-like particles with
268 a similar diameter to the D13-coated IV we imaged in situ. This strongly suggests that the
269 D13 lattice, which initially curves open membranes and eventually forms closed particles,
270 determines both the size and shape of the IV. In addition, our images and STA maps show
271 that a 5.6-nm gap separates the D13 lattice from the IV membrane. This gap is most likely
272 occupied by A17, which tethers the D13 lattice to the membrane (21, 33, 34) but whose
273 flexibility would preclude its detection on the IV membrane by cryo-ET. The lack of direct
274 contact of the D13 protein lattice with the viral membrane is reminiscent of clathrin and
275 other vesicle-forming coats in eukaryotic cells where the structural lattice does not directly
276 interact with the membrane to be deformed (35, 36). Instead, an adaptor module mediates
277 the lattice-membrane association. A mechanism by which coat complexes promote
278 membrane curvature is by clustering the adaptor module on the membrane to be deformed
279 (37, 38). Therefore, D13-mediated clustering of A17 could promote membrane deformation
280 during IV formation. In addition, A17 can also contribute to membrane bending
281 independently of D13, since it can deform membranes in vitro and when expressed in non-
282 infected cells (39).
283
284 Despite their relatively constant diameter, a proportion of D13-coated IV have an elongated
285 membrane invagination (Figure 1A). This feature has largely gone unnoticed in previous EM

286 studies imaging thin sections, although IV membrane deformations are apparent in some
287 studies (28, 40-43). While the cause of this membrane buckling remains to be established,
288 it may relate to the thinness of the cell periphery or a consequence of forces on the
289 membrane during IV assembly or DNA insertion into assembling IV (42). As in other studies,
290 we observe the nucleoid in the IV interior or associated with either open or closed spheres,
291 as previously suggested for DNA entry events (28, 30). It is tempting to speculate that the
292 IV invagination may mark the site of DNA entry and IV sealing of the pore.
293
294 The palisade, which is largely composed of p4A and A4 (31, 44, 45), consists of a trimeric
295 assembly in a pseudo-hexagonal lattice arrangement. This new viral lattice, which fully
296 covers the core and defines its boundary, also dictates the dimensions and shape of IMV.
297 The viral membrane, no longer covered by D13, wrinkles and adopts the shape and
298 dimensions of the newly formed palisade. This process may also be responsible for the
299 compression of the lateral bodies onto the virus core, causing the biconcave deformation of
300 the latter. The maturation model that emerges from our work provides a simple way by
301 which a membrane-bound particle adapts to a new internal lattice and changes its shape
302 and dimensions to become more compact without membrane removal (Figure 7D).
303 Moreover, our data suggest the palisade length is dictated by the diameter of the IV, which
304 in turn is established by D13. The palisade would grow inside the D13-coated IV until
305 reaching its maximum length, that is the IV diameter. In other words, the D13 lattice limits
306 the longest dimension of the palisade lattice. The size restriction of a growing viral core by
307 its surrounding viral membrane has also been proposed for the assembly of the HIV core (46,
308 47). Our observation of a viral particle partly coated by D13 with an assembled palisade
309 suggests removal of D13 only occurs once the palisade is fully formed (Figure 7C). Moreover,
310 our observations suggest that palisade assembly and D13 removal are coordinated and rapid.
311
312 In the IMV, the lateral bodies define a lateral domain, as opposed to the virion tips, which
313 are specified by the long axis of the viral core. The lateral bodies prevent direct interactions
314 between the palisade and the wrinkled viral membrane, which may contribute to the
315 differences between the lateral and the tip domains. Notably, the virion tips are the site of
316 polarisation of the set of viral membrane proteins that form the entry fusion complex (EFC),
317 which is essential for virus infectivity (48-50). How and when EFC polarity is established is
318 unknown. An appealing possibility is that virion tips are stochastically defined by the growth
319 of the palisade long axis during assembly and the EFC and other viral factors polarise at the
320 virion tips after palisade formation by their exclusion from the lateral domains. In such a
321 scenario, palisade formation would drive virion polarity.

322 The EFC mediates fusion of the IMV membrane with the plasma membrane or an endocytic
323 compartment during entry, which releases a naked core into the cytoplasm (51-55).
324 Subsequently, early proteins are produced by early RNA transcripts released from naked
325 cores, which are essential to liberate the DNA genome into the cytosol to initiate replication
326 (1). Our cryo-ET data of naked cores in infected cells indicate the palisade structure does
327 not require surrounding membranes for stability. Furthermore, the loss of lateral bodies
328 from naked cores suggests their association with the palisade depends on the IMV
329 membrane. In addition, we observed flexible 2.6-nm thick polymers fully surrounding naked
330 cores that might correspond to either RNA or the viral genome which is released from the
331 naked core. Finally, we detected ring structures protruding from the palisade surface of
332 naked cores. Analysis of these rings reveals they are compatible in dimension with the
333 hexameric rings of the viral D5 primase/helicase, which is essential for vaccinia genome
334 release (56, 57).
335
336 A common feature of many viral families is the use of a three-dimensional lattice, or capsid,
337 which determines the structure and dimensions of the virion. What distinguishes vaccinia
338 from other viruses is that an initial lattice, D13, is replaced by a second lattice, the palisade,
339 during virion assembly. This contrasts African Swine Fever virus (ASFV), which retains its
340 D13-like lattice, in addition to an inner capsid in mature virions (58). Based on the structural
341 similarities between D13 and the structural components of other viruses with a pseudo-
342 hexameric structure formed by a trimeric protein containing concatenated beta-barrels,
343 vaccinia has been included in the PRD1/adenovirus lineage (59). However, the viral proteins
344 that form the palisade, which is present in the mature particles, may be just as important
345 as D13 in structural phylogenetic comparisons.
346
347 The palisade is a regular capsid-like structure determining the morphology of all forms of
348 vaccinia virions (IMV, IEV, EEV and CEV). The additional membranes acquired by
349 envelopment are different to the IMV viral membrane as they are not corrugated or always
350 in close contact with the IMV surface. Moreover, the acquisition of these membranes is not
351 associated with major changes in the virion structure or palisade architecture (Figure 5).
352 This suggests that these additional membranes are used to facilitate viral egress before cell
353 lysis. In fact, these membranes and associated proteins drive IEV transport on microtubules
354 to the cell periphery, IEV fusion with the plasma membrane and subsequent actin-based
355 transport of CEV (7-11, 13). In contrast, the IMV membrane serves to contain the viral core
356 and lateral bodies and organises the essential components required for entry and, also,
357 envelopment during viral morphogenesis. Based on the strong protein conservation between

358 orthopoxviruses, we believe that the virion assembly of monkeypox and variola major are
359 likely to be identical to that of vaccinia virus we have described here.
360
361 **Methods**
362 **Recombinant viruses**
363 To facilitate cryo-electron microscopy (EM) observations, we produced recombinant
364 Western Reserve (WR) vaccinia strains lacking F11 as this prevents infected cells from
365 rounding-up early during infection (60). In addition, the A36-YdF mutation was used to
366 abolish actin tail formation beneath CEV (11, 13, 61). The F11 gene was deleted in A36 YdF
367 (8) or A36 YdF ΔNPF1-3 (62) backgrounds using the same targeting strategy as previously
368 described (63). Fluorescence was used as a selectable marker to isolate recombinant ΔF11-
369 mCherry viruses by successive rounds of plaque purification in BS-C-1 cells. Correct gene
370 replacement and complete isolation of the recombinant viral strains was confirmed by PCR,
371 sequencing of the F11 locus and western blot analysis.
372
373 **Cell growth, vaccinia infection and vitrification**
374 HeLa cells were maintained in complete MEM (supplemented with 10% Fetal Bovine Serum,
375 100 ug/ml streptomycin and 100 U/ml penicillin) at 37 °C with 5% CO_2. Cells were washed
376 with PBS, treated with trypsin, seeded on glow discharged (40 sec at 45 mA) Quantifoil
377 R3.5/1 gold grids of 200 mesh and placed in wells of 6-well plates with complete MEM. After
378 overnight growth, the cells were infected with A36 YdF ΔF11 or A36 YdF ΔNPF1-3 ΔF11
379 vaccinia virus strains in serum-free MEM at a multiplicity of infection of 2. After one hour,
380 the medium was replaced with complete MEM. At 8 hours post infection the grids were
381 washed once with PBS and excess PBS was removed with a Whatman paper before blotting
382 and vitrification using the Vitrobot Mark IV System, which was set to 95% relative humidity
383 at 22 °C. Colloidal gold particles (10-nm diameter) were pipetted onto grids before blotting,
384 which was performed for 14 s with a relative force of -10.
385
386 **Cryo-electron tomography, image processing and analyses**
387 Grids were first screened on a Talos Arctica TEM (Thermo Fisher) to select edges of cells
388 with an abundance of viral particles that were thin enough for cryo-ET. The precise location
389 of the selected regions on each grid was registered. The grids were subsequently transferred
390 to a Titan Krios (Thermo Fisher) and the mapped grid selections were re-imaged. The Titan
391 Krios was fitted with a K2 Summit direct detector (Gatan) operated in electron counting
392 mode. A Gatan GIF energy filter was used in zero-loss mode with a 20 eV slit width. Dose-
393 symmetric tilt series were collected from -57° to +57° at a 3° increment, a pixel size of

394 4.31 Å and a defocus of -8 µm using Tomography 5.7 software (Thermo Fisher) (Table S2).
395 Four movie frames were collected per tilt with a dose of 1.7 e / Å^2 per tilt, giving a
396 cumulative dose of 66.3 e / Å^2 per tilt series. Movie frames were aligned using alignframes
397 from IMOD (64). Tilt series were aligned using 10-nm Au fiducials or patch tracking in IMOD.
398 Contrast transfer function (CTF) correction and tomogram reconstruction were also
399 implemented in IMOD (64, 65). Alternatively, tomograms were CTF corrected and
400 reconstructed using novaCTF (66). In both cases, a SIRT-like filter equivalent to 5 iterations
401 was routinely applied. Tomogram segmentations were manually performed using AMIRA
402 (Thermo Fisher), mainly using tomograms that were further denoised using ISONet with CTF
403 deconvolution and missing-wedge filling from deep learning (67).
404
405 The diameter of IV, the axes of IMV and their perimeters, and the major axes of IEV and EEV
406 were measured in 3dmod from IMOD using a middle plane of each viral particle. For
407 perimeters, the viral membranes were manually traced to measure their total contour
408 length. As reported previously (23), virions with their dumbbell side view perpendicular to
409 the electron beam were much less frequent than other views. Because of this, for the
410 calculation of the minor axis of IMV we measured the minor axis of both IMV and IMV inside
411 EEV. This is also the reason why we did not find enough side views of IEV to directly measure
412 their minor axis (Table S1). To estimate the IEV minor axis, we measured the thickness that
413 the additional IEV membranes add, and combined it to the calculated IMV minor axis. For
414 volumes calculation, we assumed IV are perfectly spherical and IMV, IEV and EEV triaxial
415 elipsoids.
416
417 **Subtomogram averaging**
418 Tomograms containing IV or IMV were selected for subtomogram averaging (STA). D13 and
419 palisade particles in immature and mature virions respectively were picked from the bin4
420 SIRT-filtered tomograms using oversampled surface models in Dynamo (68), then imported
421 to Relion 3.1 (69) for subsequent subtomogram averaging. Unless otherwise specified, local
422 angular searches about the initial orientations generated in Dynamo were used throughout
423 data processing. For particle extraction, only unbinned weighted back projections
424 reconstructions from novaCTF were used. Lattice measurements were carried out in real
425 space using ChimeraX (70). D13 particles were extracted in 96-pixel boxes at the bin2 pixel
426 size of 4.31Å/pixel. An initial reference was generated using reference-free 3D classification
427 without applied symmetry, with the resulting map clearly showing the honeycomb lattice
428 of D13 trimers. Initial classification and refinement was carried out in both C1 and C6
429 symmetries to verify the symmetry of the D13 hexamer-of-trimers. After initial

430 classifications and removing of overlapping particles with a distance cutoff of 50Å, particles
431 were re-extracted without binning (4.31Å/pixel) in 192 pixel boxes. Final refinement in C6
432 symmetry reached 19Å resolution according to the FSC=0.143 criterion.
433
434 Palisade particles were initially extracted at binning level 2 (8.62Å/pixel) in 96-pixel boxes.
435 Initial references were generated using independent reference-free 3D classifications for
436 each virion type. This clearly showed the palisade lattice in every case, and the particles
437 for each virion type were from then on processed independently, but in an identical manner.
438 For each virion type, alternating rounds of 3D classification and refinement were used to
439 centre the palisade particles at 2-fold binning. After convergence at 2-fold binning, particles
440 were re-extracted without binning (4.31Å/pixel) in 128-pixel boxes. Overlapping particles
441 were removed with a distance cutoff of 40Å before further refinements were carried out
442 without binning. As all refinements converged on maps with identical lattices, particles from
443 all virion types except for the naked cores were then combined for further refinements. All
444 refinements were carried out without application of symmetry up to this point. After the
445 C1 maps converged and the symmetry of the lattice was apparent, further refinement runs
446 were carried out with C3 symmetry applied. The final resolutions of the palisade maps
447 ranged from 20-30Å, according to the FSC=0.143 criterion.
448
449 **Immunofluorescence imaging**
450 HeLa cells were plated on fibronectin-coated coverslips and infected with an RFP-A3
451 vaccinia strain (71) for 8 hours and fixed with 4% paraformaldehyde in PBS for 10 min, then
452 permeabilised with 0.1% Triton X-100 in PBS for 5 min and incubated in blocking buffer (10
453 mM MES pH 6.1, 150 mM NaCl, 5 mM EGTA, 5 mM $MgCl_2$, and 5 mM glucose) containing 2%
454 (v/v) fetal calf serum and 1% (w/v) BSA for 30 min prior to addition of 4′,6-diamidino-2-
455 phenylindole (DAPI) for 5 minutes, before mounting the coverslips using Mowiol. Coverslips
456 were imaged on an Olympus iX83 Microscope with Olympus 150x/1.45 NA X-Line
457 Apochromatic Objective Lens, dual Photometrics BSI-Express sCMOS cameras and CoolLED
458 pE-300 Light Source (Visitech) and was controlled using Micro-Manager 2.0.0. Image stacks
459 of 10-15 z-slices with 0.1 µm steps were acquired and deconvolved using the express
460 deconvolution setting on Huygens Software (Scientific Volume Imaging).
461
462 **Acknowledgements**
463 We thank Alessandro Costa, Neil McDonald and Jeremy Carlton (Francis Crick Institute) as
464 well as the Way lab for insightful comments on the manuscript as well as LuYan Cao for
465 providing the initial slide of infected cells used in our SIM analysis (Fig. 2F). We also

466 acknowledge Philip Walker and Andy Purkiss of the Structural Biology Science Technology
467 Platform and the Scientific Computing Science Technology Platform for computational
468 support. MHG also thanks Pauline McIntosh (Francis Crick Institute) for guidance during the
469 initial stages of the project. The work in the Way and Rosenthal labs was supported by the
470 Francis Crick Institute, which receives its core funding from Cancer Research UK (FC001209
471 and FC001143), the UK Medical Research Council (FC001209 and FC001143), and the
472 Wellcome Trust (FC001209 and FC001143). The funders had no role in study design, data
473 collection and analysis, decision to publish, or preparation of the manuscript. For the
474 purpose of Open Access, the authors have applied a CC BY public copyright license to any
475 Author Accepted Manuscript version arising from this submission.
476

477 **Author contributions**

478 All authors designed the research program and strategy. MHG, TC and AN performed
479 research, MHG and TC analyzed data and MHG, TC, PBR and MW wrote the paper.
480

481 **Competing interests**

482 The authors have no competing financial interests
483

484 **References**

485 1. B. Moss, "Poxviridae: the viruses and their replication" in Fields Virology, H. P. Knipe
486 DM, Ed. (Lippincott Williams and Wilkins, Philadelphia, 2007), pp. 2905-2946.
487 2. B. L. Jacobs *et al.*, Vaccinia virus vaccines: past, present and future. *Antiviral Res*
488 **84**, 1-13 (2009).
489 3. S. R. Walsh, R. Dolin, Vaccinia viruses: vaccines against smallpox and vectors against
490 infectious diseases and tumors. *Expert Rev Vaccines* **10**, 1221-1240 (2011).
491 4. K. L. Roberts, G. L. Smith, Vaccinia virus morphogenesis and dissemination. *Trends*
492 *Microbiol* **16**, 472-479 (2008).
493 5. M. Schmelz *et al.*, Assembly of vaccinia virus: the second wrapping cisterna is derived
494 from the trans Golgi network. *J Virol* **68**, 130-147 (1994).
495 6. J. Tooze, M. Hollinshead, B. Reis, K. Radsak, H. Kern, Progeny vaccinia and human
496 cytomegalovirus particles utilize early endosomal cisternae for their envelopes. *Eur J Cell*
497 *Biol* **60**, 163-178 (1993).
498 7. G. L. Smith, A. Vanderplasschen, M. Law, The formation and function of extracellular
499 enveloped vaccinia virus. *J Gen Virol* **83**, 2915-2931 (2002).
500 8. J. Rietdorf *et al.*, Kinesin-dependent movement on microtubules precedes actin-
501 based motility of vaccinia virus. *Nat Cell Biol* **3**, 992-1000 (2001).

502 9. F. Leite, M. Way, The role of signalling and the cytoskeleton during Vaccinia Virus
503 egress. *Virus Res* **209**, 87-99 (2015).
504 10. S. Cudmore, P. Cossart, G. Griffiths, M. Way, Actin-based motility of vaccinia virus.
505 *Nature* **378**, 636-638 (1995).
506 11. F. Frischknecht *et al.*, Actin-based motility of vaccinia virus mimics receptor tyrosine
507 kinase signalling. *Nature* **401**, 926-929 (1999).
508 12. M. Hollinshead *et al.*, Vaccinia virus utilizes microtubules for movement to the cell
509 surface. *J Cell Biol* **154**, 389-402 (2001).
510 13. B. M. Ward, B. Moss, Vaccinia virus intracellular movement is associated with
511 microtubules and independent of actin tails. *J Virol* **75**, 11651-11663 (2001).
512 14. A. S. Weisberg *et al.*, Enigmatic origin of the poxvirus membrane from the
513 endoplasmic reticulum shown by 3D imaging of vaccinia virus assembly mutants. *Proc Natl*
514 *Acad Sci U S A* **114**, E11001-E11009 (2017).
515 15. B. Moss, Poxvirus membrane biogenesis. *Virology* **479-480**, 619-626 (2015).
516 16. P. Chlanda, M. A. Carbajal, M. Cyrklaff, G. Griffiths, J. Krijnse-Locker, Membrane
517 rupture generates single open membrane sheets during vaccinia virus assembly. *Cell Host*
518 *Microbe* **6**, 81-90 (2009).
519 17. J. Heuser, Deep-etch EM reveals that the early poxvirus envelope is a single
520 membrane bilayer stabilized by a geodetic "honeycomb" surface coat. *J Cell Biol* **169**, 269-
521 283 (2005).
522 18. P. Szajner, A. S. Weisberg, J. Lebowitz, J. Heuser, B. Moss, External scaffold of
523 spherical immature poxvirus particles is made of protein trimers, forming a honeycomb
524 lattice. *J Cell Biol* **170**, 971-981 (2005).
525 19. J. Hyun, H. Matsunami, T. G. Kim, M. Wolf, Assembly mechanism of the pleomorphic
526 immature poxvirus scaffold. *Nat Commun* **13**, 1704 (2022).
527 20. M. W. Bahar, S. C. Graham, D. I. Stuart, J. M. Grimes, Insights into the evolution of
528 a complex virus from the crystal structure of vaccinia virus D13. *Structure* **19**, 1011-1020
529 (2011).
530 21. D. Garriga *et al.*, Structural basis for the inhibition of poxvirus assembly by the
531 antibiotic rifampicin. *Proc Natl Acad Sci U S A* **115**, 8424-8429 (2018).
532 22. J. K. Hyun *et al.*, Membrane remodeling by the double-barrel scaffolding protein of
533 poxvirus. *PLoS Pathog* **7**, e1002239 (2011).
534 23. R. C. Condit, N. Moussatche, P. Traktman, In a nutshell: structure and assembly of
535 the vaccinia virion. *Adv Virus Res* **66**, 31-124 (2006).
536 24. C. Ansarah-Sobrinho, B. Moss, Role of the I7 protein in proteolytic processing of
537 vaccinia virus membrane and core components. *J Virol* **78**, 6335-6343 (2004).

538 25. T. G. Senkevich, C. L. White, E. V. Koonin, B. Moss, Complete pathway for protein
539 disulfide bond formation encoded by poxviruses. *Proc Natl Acad Sci U S A* **99**, 6667-6672
540 (2002).
541 26. M. Cyrklaff *et al.*, Cryo-electron tomography of vaccinia virus. *Proc Natl Acad Sci U*
542 *S A* **102**, 2772-2777 (2005).
543 27. J. Dubochet, M. Adrian, K. Richter, J. Garces, R. Wittek, Structure of intracellular
544 mature vaccinia virus observed by cryoelectron microscopy. *J Virol* **68**, 1935-1941 (1994).
545 28. G. Griffiths, N. Roos, S. Schleich, J. K. Locker, Structure and assembly of
546 intracellular mature vaccinia virus: thin-section analyses. *J Virol* **75**, 11056-11070 (2001).
547 29. A. R. Mohandas, S. Dales, Involvement of spicules in the formation of vaccinia virus
548 envelopes elucidated by a conditional lethal mutant. *Virology* **214**, 494-502 (1995).
549 30. C. Morgan, The insertion of DNA into vaccinia virus. *Science* **193**, 591-592 (1976).
550 31. N. Roos *et al.*, A novel immunogold cryoelectron microscopic approach to investigate
551 the structure of the intracellular and extracellular forms of vaccinia virus. *EMBO J* **15**, 2343-
552 2355 (1996).
553 32. M. Cyrklaff *et al.*, Whole cell cryo-electron tomography reveals distinct disassembly
554 intermediates of vaccinia virus. *PLoS One* **2**, e420 (2007).
555 33. B. Unger, J. Mercer, K. A. Boyle, P. Traktman, Biogenesis of the vaccinia virus
556 membrane: genetic and ultrastructural analysis of the contributions of the A14 and A17
557 proteins. *J Virol* **87**, 1083-1097 (2013).
558 34. H. Bisht, A. S. Weisberg, P. Szajner, B. Moss, Assembly and disassembly of the capsid-
559 like external scaffold of immature virions during vaccinia virus morphogenesis. *J Virol* **83**,
560 9140-9150 (2009).
561 35. M. Faini, R. Beck, F. T. Wieland, J. A. Briggs, Vesicle coats: structure, function, and
562 general principles of assembly. *Trends Cell Biol* **23**, 279-288 (2013).
563 36. T. Kirchhausen, Three ways to make a vesicle. *Nat Rev Mol Cell Biol* **1**, 187-198
564 (2000).
565 37. J. C. Stachowiak, F. M. Brodsky, E. A. Miller, A cost-benefit analysis of the physical
566 mechanisms of membrane curvature. *Nat Cell Biol* **15**, 1019-1027 (2013).
567 38. J. C. Stachowiak *et al.*, Membrane bending by protein-protein crowding. *Nat Cell*
568 *Biol* **14**, 944-949 (2012).
569 39. K. J. Erlandson *et al.*, Poxviruses Encode a Reticulon-Like Protein that Promotes
570 Membrane Curvature. *Cell Rep* **14**, 2084-2091 (2016).
571 40. B. Sodeik *et al.*, Assembly of vaccinia virus: role of the intermediate compartment
572 between the endoplasmic reticulum and the Golgi stacks. *J Cell Biol* **121**, 521-541 (1993).

573 41. J. R. Rodriguez, C. Risco, J. L. Carrascosa, M. Esteban, D. Rodriguez, Vaccinia virus
574 15-kilodalton (A14L) protein is essential for assembly and attachment of viral crescents to
575 virosomes. *J Virol* **72**, 1287-1296 (1998).
576 42. M. Ericsson *et al.*, Characterization of ts 16, a temperature-sensitive mutant of
577 vaccinia virus. *J Virol* **69**, 7072-7086 (1995).
578 43. W. W. Yeh, B. Moss, E. J. Wolffe, The vaccinia virus A9L gene encodes a membrane
579 protein required for an early step in virion morphogenesis. *J Virol* **74**, 9701-9711 (2000).
580 44. S. Cudmore *et al.*, A vaccinia virus core protein, p39, is membrane associated. *J*
581 *Virol* **70**, 6909-6921 (1996).
582 45. S. Wilton, A. R. Mohandas, S. Dales, Organization of the vaccinia envelope and
583 relationship to the structure of intracellular mature virions. *Virology* **214**, 503-511 (1995).
584 46. J. A. Briggs *et al.*, The mechanism of HIV-1 core assembly: insights from three-
585 dimensional reconstructions of authentic virions. *Structure* **14**, 15-20 (2006).
586 47. J. A. Briggs, T. Wilk, R. Welker, H. G. Krausslich, S. D. Fuller, Structural organization
587 of authentic, mature HIV-1 virions and cores. *EMBO J* **22**, 1707-1715 (2003).
588 48. R. D. M. Gray *et al.*, Nanoscale polarization of the entry fusion complex of vaccinia
589 virus drives efficient fusion. *Nat Microbiol* **4**, 1636-1644 (2019).
590 49. T. G. Senkevich, B. M. Ward, B. Moss, Vaccinia virus entry into cells is dependent on
591 a virion surface protein encoded by the A28L gene. *J Virol* **78**, 2357-2366 (2004).
592 50. B. Moss, Poxvirus cell entry: how many proteins does it take? *Viruses* **4**, 688-707
593 (2012).
594 51. F. I. Schmidt, C. K. Bleck, A. Helenius, J. Mercer, Vaccinia extracellular virions enter
595 cells by macropinocytosis and acid-activated membrane rupture. *EMBO J* **30**, 3647-3661
596 (2011).
597 52. J. Mercer, A. Helenius, Vaccinia virus uses macropinocytosis and apoptotic mimicry
598 to enter host cells. *Science* **320**, 531-535 (2008).
599 53. R. A. Janeczko, J. F. Rodriguez, M. Esteban, Studies on the mechanism of entry of
600 vaccinia virus in animal cells. *Arch Virol* **92**, 135-150 (1987).
601 54. G. C. Carter, M. Law, M. Hollinshead, G. L. Smith, Entry of the vaccinia virus
602 intracellular mature virion and its interactions with glycosaminoglycans. *J Gen Virol* **86**,
603 1279-1290 (2005).
604 55. R. W. Doms, R. Blumenthal, B. Moss, Fusion of intra- and extracellular forms of
605 vaccinia virus with the cell membrane. *J Virol* **64**, 4884-4892 (1990).
606 56. S. Kilcher *et al.*, siRNA screen of early poxvirus genes identifies the AAA+ ATPase D5
607 as the virus genome-uncoating factor. *Cell Host Microbe* **15**, 103-112 (2014).

608 57. S. Hutin *et al.*, Domain Organization of Vaccinia Virus Helicase-Primase D5. *J Virol*
609 **90**, 4604-4613 (2016).
610 58. N. Wang *et al.*, Architecture of African swine fever virus and implications for viral
611 assembly. *Science* **366**, 640-644 (2019).
612 59. N. G. Abrescia, D. H. Bamford, J. M. Grimes, D. I. Stuart, Structure unifies the viral
613 universe. *Annu Rev Biochem* **81**, 795-822 (2012).
614 60. C. H. Durkin *et al.*, RhoD Inhibits RhoC-ROCK-Dependent Cell Contraction via PAK6.
615 *Dev Cell* **41**, 315-329 e317 (2017).
616 61. H. Lynn *et al.*, Loss of cytoskeletal transport during egress critically attenuates
617 ectromelia virus infection in vivo. *J Virol* **86**, 7427-7443 (2012).
618 62. X. Snetkov, I. Weisswange, J. Pfanzelter, A. C. Humphries, M. Way, NPF motifs in
619 the vaccinia virus protein A36 recruit intersectin-1 to promote Cdc42:N-WASP-mediated
620 viral release from infected cells. *Nat Microbiol* **1**, 16141 (2016).
621 63. J. V. Cordeiro *et al.*, F11-mediated inhibition of RhoA signalling enhances the spread
622 of vaccinia virus in vitro and in vivo in an intranasal mouse model of infection. *PLoS One* **4**,
623 e8506 (2009).
624 64. J. R. Kremer, D. N. Mastronarde, J. R. McIntosh, Computer visualization of three-
625 dimensional image data using IMOD. *J Struct Biol* **116**, 71-76 (1996).
626 65. Q. Xiong, M. K. Morphew, C. L. Schwartz, A. H. Hoenger, D. N. Mastronarde, CTF
627 determination and correction for low dose tomographic tilt series. *J Struct Biol* **168**, 378-
628 387 (2009).
629 66. B. Turonova, F. K. M. Schur, W. Wan, J. A. G. Briggs, Efficient 3D-CTF correction for
630 cryo-electron tomography using NovaCTF improves subtomogram averaging resolution to
631 3.4A. *J Struct Biol* **199**, 187-195 (2017).
632 67. Y.-T. Liu *et al.*, Isotropic Reconstruction of Electron Tomograms with Deep Learning.
633 *bioRxiv* 10.1101/2021.07.17.452128, 2021.2007.2017.452128 (2021).
634 68. D. Castano-Diez, M. Kudryashev, H. Stahlberg, Dynamo Catalogue: Geometrical tools
635 and data management for particle picking in subtomogram averaging of cryo-electron
636 tomograms. *J Struct Biol* **197**, 135-144 (2017).
637 69. T. A. M. Bharat, C. J. Russo, J. Lowe, L. A. Passmore, S. H. W. Scheres, Advances in
638 Single-Particle Electron Cryomicroscopy Structure Determination applied to Sub-tomogram
639 Averaging. *Structure* **23**, 1743-1753 (2015).
640 70. E. F. Pettersen *et al.*, UCSF ChimeraX: Structure visualization for researchers,
641 educators, and developers. *Protein Sci* **30**, 70-82 (2021).

642 71. I. Weisswange, T. P. Newsome, S. Schleich, M. Way, The rate of N-WASP exchange
643 limits the extent of ARP2/3-complex-dependent actin-based motility. *Nature* **458**, 87-91
644 (2009).
645
646
647 **Legends**
648 **Figure 1. Cryo-ET of vaccinia infected cells.**
649 **A**. Schematic representation of the different stages in vaccinia assembly and envelopment.
650 D13 coated membrane crescents initially close to form a spherical IV, that mature into brick
651 shaped IMV with dumbbell shaped viral core flanked by two lateral bodies (red).
652 Envelopment of IMV by a Golgi membrane cisterna or endosomal compartment (green)
653 results in the formation of triple membraned IEV, which can fuse with the plasma membrane
654 to liberate extracellular enveloped virions (EEV), which are called CEV if they remain
655 attached to the surface of the cell. **B.** Left: Central section of a tomogram showing fully
656 formed IV. The red arrow points at an IV with a lateral invagination. Invaginations in other
657 IV can be seen in the 3D-segmented model of the membrane of the same tomogram (right)
658 (See Movie 1). **C.** Tomogram middle view (left) and its corresponding segmentation (right)
659 of IMV (See Movie 2). A "cut corner" (magenta arrows) is apparent in some IMV. Scalebars =
660 100 nm.
661
662 **Figure 2. The stages of IV assembly**
663 **A.** Tomogram section showing D13 coated membrane crescents with open ends (indicated
664 magenta arrowheads). **B.** Tomogram sections showing the last stages of IV membrane
665 closure: the middle view (left) reveals membrane discontinuity (indicated magenta
666 arrowheads) while in the higher plane at + 48 nm relative to the middle view (right) the
667 membrane is continuous (see Movie 3). **C.** Closed IV containing a condensed nucleoid
668 (outlined in magenta) with repeated structural features (magenta arrowheads). **D.**
669 Cytoplasmic condensed nucleoid/s next to an IV. **E.** Extended nucleoid/s in association with
670 an open IV. **F.** Structured illumination microscopy image of infected cell showing condensed
671 DNA structures (green) in association with RFP-A3 positive viral particles (magenta) located
672 in a perinuclear viral factory. Tomogram Scalebars = 100 nm.
673
674 **Figure 3. In situ structure of the D13 lattice.**
675 **A.** Tomogram section as indicated in the schematic on the left through the middle and top
676 of a representative IV (see Movie 4). The densities corresponding to the D13 lattice are
677 coloured in magenta in panels (right) and show pseudo-hexagonal organisation. Scale bar =

678 100 nm. **B.** Map based on subtomogram averaging of D13 and the underlying IV membrane
679 from a top (left) and a side (right) view with fitting of coordinate models of D13 trimers(PDB
680 7VFE) shown in blue/brown.
681
682 **Figure 4. Ultrastructure of IMV.**
683 **A.** Central plane of a tomogram showing the broadest view of a representative IMV together
684 with a region magnified 2.5-times to highlight the outer layer, viral membrane, palisade
685 and inner wall of the virion (see Movie 5). **B.** Lateral view of an IMV, showing the lateral
686 bodies (outlined in red) and the dumbbell shape of the core. The magnified regions outlined
687 in magenta show the same characteristic IMV layers. **C.** Different sections of the IMV shown
688 in A at the indicated plane positions in nm. The insert in the +31 nm view shows the surface
689 of the palisade lattice. In the second row, yellow highlights the palisade structure, while
690 red indicates the lateral body in the +52 nm view. **D.** The first row shows a schematic
691 representation of the views displayed in C, while the second row represents the orthogonal
692 view together with the tomogram position (black line). **E.** Left: Top and side views of a
693 segmentation model of the IMV in A. The outer layer (blue) and viral membrane (black) are
694 cut away so the internal palisade (yellow) and the lateral bodies (red) can be seen (see
695 Movie 6). Right: The dumbbell shaped core is more apparent in a Simulated Digitally
696 Reconstructed Radiograph (DDR Rendering) of the same segmentation model. Scale bars =
697 100 nm.
698
699 **Figure 5. Ultrastructure of the naked viral core.**
700 **A.** Middle section of a tomogram showing a naked viral core together with a region
701 magnified 3 times to highlight the palisade and inner wall as well as the polymers that
702 surround the core. **B.** A higher tomogram section (+ 41 nm) of the same naked viral core
703 highlighting the pseudohexagonal lattice of the palisade. **C.** At an even higher section (+58
704 nm) ring structures associated with the palisade are evident. The dimensions of the rings
705 (n=25) from 5 naked cores are indicated together with the standard error of the mean. Scale
706 bars = 100 nm.
707
708 **Figure 6. The palisade is a pseudohexagonal lattice composed of trimeric proteins.**
709 **A.** Central plane of a tomograms showing that the additional membranes of IEV and CEV
710 (associated with the plasma membrane, PM) do not alter the ultrastructure of the internal
711 IMV. Scale bar = 100 nm. **B.** Schematic representation to illustrate the number of membranes
712 of IMV, IEV and EEV/CEV. **C.** Sections through the palisade layer corresponding to the virions
713 shown in A. Scale bar = 10 nm. **D.** Map derived from subtomogram averaging showing the

714 inner wall, palisade layer, viral membrane, and outer layer in surface representation (left)
715 and corresponding sections of the map (right).
716
717 **Figure 7. Maturation of vaccinia virus: from IV to IMV.**
718 **A.** Table showing the measured dimensions of middle views of IV (diameter, n = 26;
719 perimeter, n = 15) and IMV (major axis, n = 22; intermediate axis, n = 19; minor axis, n =
720 10; perimeter, n = 19) tomograms. * indicates that the IMV minor axis was calculated from
721 the side views of 3 IMV and 7 IMV inside EEV (see methods for explanation). For volume
722 calculation IV and IMV were assumed to be spheres and triaxial ellipsoids respectively. **B.**
723 Plots showing the individual values for perimeter and diameter / major axis (indicated by
724 magenta lines in schematics below graph) of the IV, IMV and EEV. IV and IMV measurements
725 were used to calculate the averages shown in A. The averages of the EEV inner most
726 membrane perimeter and major axis are 1074.46 nm ± 7.09 nm and 348.91 ± 1.87 nm,
727 respectively. **C.** Central sections of IV and IMV along with possible intermediates together
728 with magnified regions (2.5-times) highlighting the different layers of each particle. Scale
729 bar = 100 nm. **D.** Vaccinia maturation model: the palisade lattice (yellow) forms inside D13-
730 coated IV, its maximum length being determined by the IV diameter. Following disassembly
731 of the D13 lattice, the viral membrane acquires the shape of the palisade and becomes
732 wrinkled. During this process, the presence of two lateral bodies (red) results in the
733 deformation of the core so it adopts its characteristic biconcave shape.
734
735 **Supplementary Table 1. Measurements and calculations of virion dimensions.**
736 **A.** The middle-view perimeters, IV diameter, the major axis of IMV and EEV/CEV are shown,
737 together with the standard error of the mean (SEM) and the number of viral particles
738 measured. The intermediate and minor axes of IMV are also shown, as well as the IEV axes.
739 Finally, the calculated volume of IV, IMV and IEV are provided. See Methods for details of
740 dimension calculations. **B**. For the thickness of the inner wall and the outer layer, 5
741 different IMV were measured by tracing 5 different lines for each IMV, which correspond to
742 the five measurements shown. To estimate the distance between the palisade and the viral
743 membrane (with no lateral bodies) 5 IMV were used. For the distance between the palisade
744 and the plasma membrane through lateral bodies 1 IMV and 4 EEV were included in the
745 quantification. All values correspond to nm.
746
747 **Supplementary Table 2. Cryo-ET data collection and STA processing.**
748

749 **Supplementary Figure 1. Low-magnification images of vaccinia infected HeLa cells on**
750 **grids. A**. The pink circle marks the position where the IV in Figure 1B were imaged. The
751 image on the right is a magnification of the circled area and its surroundings. **B**. A cryo-EM
752 image showing IV (magenta arrow) and IMV (green arrow) visualised at low magnification in
753 cells over holes in the carbon support film. Scale bars = 10 (left) and 1 µm (right) (A) and 1
754 µm (B).
755
756 **Supplementary Figure 2. Tomographic gallery of IV with nucleoids**
757 Tomographic sections showing IV with an internal condensed nucleoid outlined in magenta
758 in the bottom row. Scale bar = 100 nm.
759
760 **Supplementary Figure 3. Examples of IMV with cut corners**
761 Gallery of tomographic sections of IMV showing cut or flattened corner/s (black
762 arrowheads). Scale bar = 100 nm.
763
764 **Supplementary Figure 4. Palisade maps from IMV, IEV and EEV/CEV.**
765 **A**. Maps derived from subtomogram averaging IMV, IEV or EEV/CEV. A surface (top) and a
766 cut-section view (bottom) are shown. **B**. Fourier Shell Correlation plots for palisade maps as
767 well as for the D13 map. Curves are given for the corrected, unmasked, masked and masked
768 with phase randomisations calculations.
769
770 **Movie 1. IV overview.**
771 Tomogram of an intracellular region accumulating IV, which corresponds to the section
772 shown in Figure 1B. IV membranes are segmented in red
773
774 **Movie 2. IMV overview**.
775 Tomogram showing IMV in the cytoplasm, which corresponds to the section shown in Figure
776 1C. IMV membrane is segmented in blue, microtubules in red and the lumen of an ER-like
777 compartment in yellow.
778
779 **Movie 3. IV assembly.** Tomogram of an IV with a pore on the viral membrane (pore labelled
780 with magenta arrowheads). Sections of this tomograms are shown in Figure 2B.
781
782 **Movie 4. Ultrastructure of IV.**
783 Tomogram corresponding to the IV shown in Figure 3A. Scale bar = 100 nm.
784

Movie 5. Ultrastructure of IMV.

Tomogram of the IMV particle shown in Figure 4A. Scale bar = 100 nm.

Movie 6. Segmentation of an IMV. The movie shows the segmentation performed on the IMV from Figure 4A. Blue is the outer layer and black labels the viral membrane, while yellow corresponds to the palisade lattice and red to the lateral bodies.

Movie 7. Ultrastructure of the naked viral core.

Tomogram of the naked core shown in Figure 5. The central magenta square marks part of the palisade, the top magenta rectangle highlights the flexible polymer observed and the small magenta squares at the end of the movie outline the ring-like structures protruding from the palisade. Scale bar = 100 nm.

821 **Supplementary Table 1. Measurements and calculations of virion dimensions.**

822

823 **A.**

Middle view perimeter	Average (nm)	SEM	
IV	1106.39	8.58	n = 15
IMV	1087.75	11.25	n = 19
EEV / CEV	1074.46	7.09	n = 20

824

825

Diameter / major axis	Average (nm)	Standard Error of the Mean (SEM)	
IV	351.89	2.88	n = 26
IMV	351.70	3.31	n = 22
EEV / CEV	348.91	1.87	n = 22

826

827

IMV	Average (nm)	SEM	
Intermediate axis	280.53	3.66	n = 19
Minor axis*	198.04	4.94	n = 10 (3 IMV, 7 EEV)

828

829

IEV	Average (nm)	SEM	
Major axis	437.86	13.88	n = 7
Intermediate axis	383.45112	10.95	n = 7
Minor axis (estimation)	259.11		

830

831

	Calculated volume (nm^3)
IV	2.28×10^7
IMV	1.02×10^7
IEV	2.28×10^7

832

833

834

835

836

837 **B.**

Inner wall thickness (nm)	IMV1	IMV2	IMV3	IMV4	IMV5			
1	4.89	4.12	2.08	4.43	3.72			
2	4.29	3.88	4.28	3.20	2.71			
3	3.54	4.21	4.75	3.11	4.78			
4	3.25	3.48	3.61	2.38	4.28	Final average	Standard Deviation	SEM
5	3.91	4.02	2.81	6.05	4.20			
average	3.98	3.94	3.51	3.84	3.94	3.84	0.19	0.09

838

Outer layer thickness (nm)	IMV1	IMV2	IMV3	IMV4	IMV5			
1	7.24	8.15	6.14	6.90	5.61			
2	7.51	7.14	7.25	6.52	7.31			
3	7.48	6.55	5.86	6.37	5.05			
4	6.40	7.12	6.03	6.96	6.63	Final average	Standard Deviation	SEM
5	5.58	5.77	7.71	6.28	7.11			
average	6.84	6.95	6.60	6.61	6.34	6.67	0.11	0.24

839

Palisade-to-viral membrane distance (nm)	IMV1	IMV3	IMV4	IMV5			
1	9.54	10.12	8.89	9.47			
2	9.57	9.37	7.87	8.08			
3	11.18	9.51	8.32	8.31	Final average	Standard Deviation	SEM
4	8.89	9.57	11.28	10.98			
5	8.66	8.53	7.36	10.04			
average	9.57	9.42	8.74	9.38	9.28	0.18	0.36

840

Palisade to viral membrane through lateral bodies (nm)	IMV1	EEV1	EEV2	EEV3	EEV4	Average	Standard Deviation	SEM
1	53.20	50.35	43.45	52.01	41.76			
2	31.93	48.19	42.39	62.64	39.35	46.53	8.60	2.72

841

842 **Supplementary Table S2. Cryo-ET data collection and STA processing.**

843

	Palisade				D13
	Combined	EEV/CEV	IMV	IEV	
Data collection					
Voltage (kV)	300				
Cumulative electron dose (e / $Å^2$)	66.3				
Applied defocus (µm)	-8				
Pixel size (Å)	4.31				
Tilt range (°)	±57°, dose symmetric				
STA processing					
Map symmetry	C3	C3	C3	C3	C6
Initial particle number	182938	209703	80698	8256	341376
Final particle number	179822	149662	27590	5686	34092
Map resolution (Å) (FSC=0.143)	21.2	21.2	25.1	30.6	19.2

844

845

A

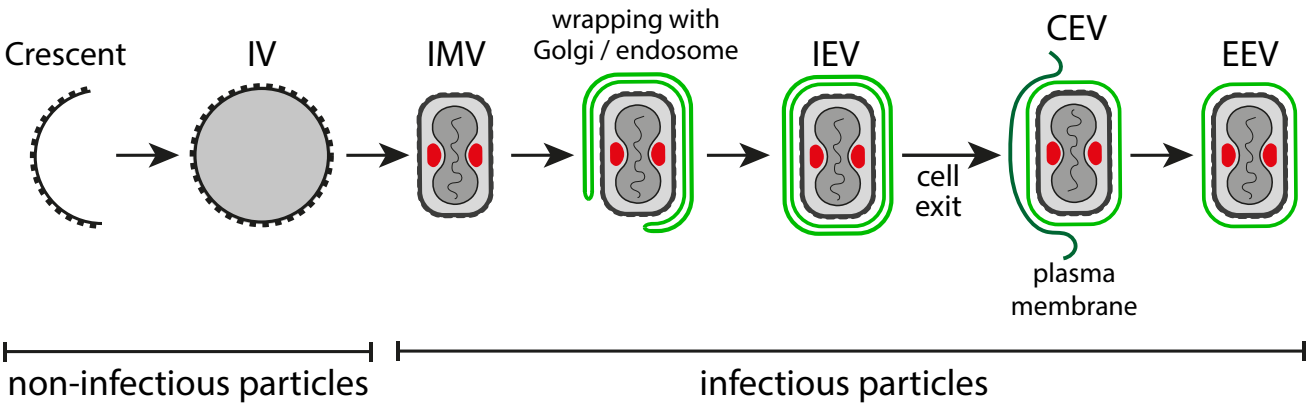
Crescent
IV
IMV
wrapping with
Golgi / endosome
IEV
cell
exit
CEV
plasma
membrane
EEV
non-infectious particles
infectious particles

B

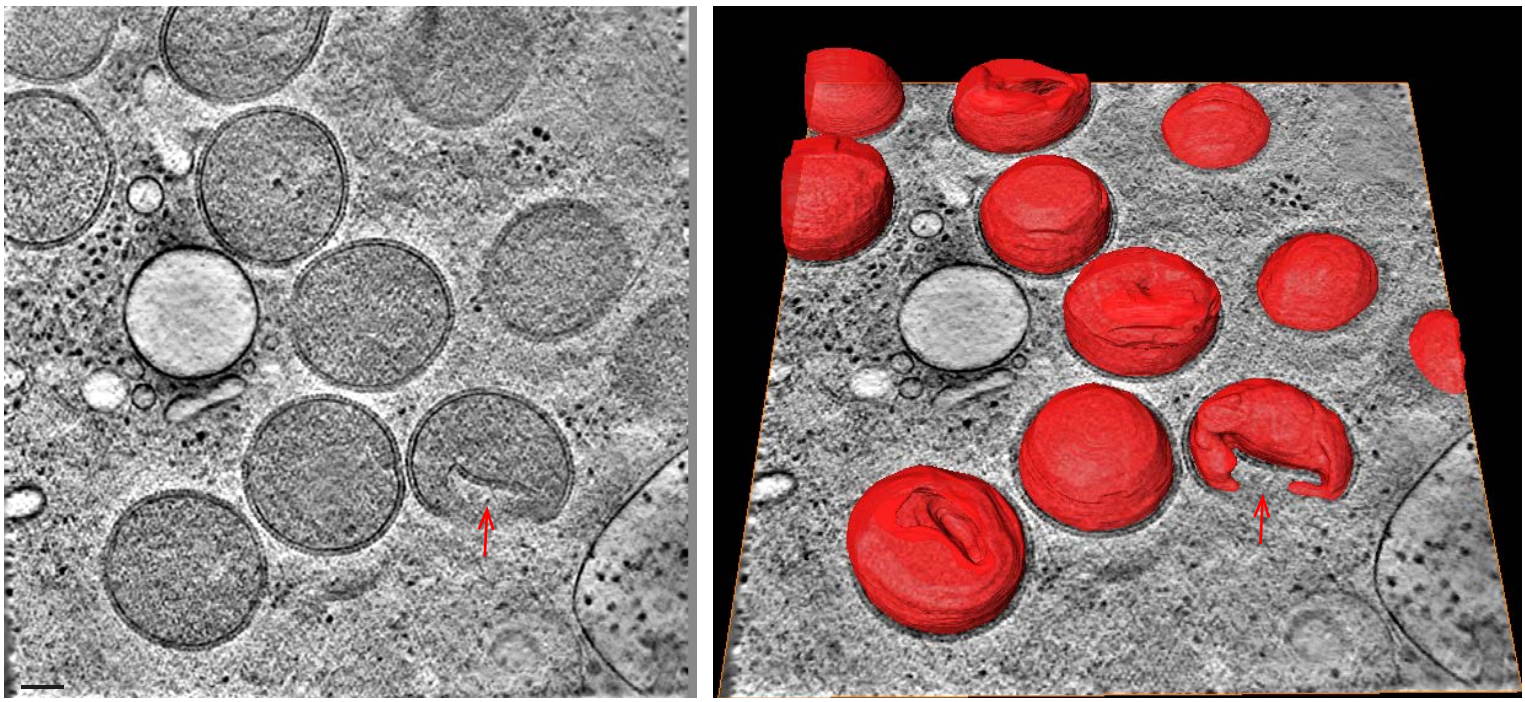

C

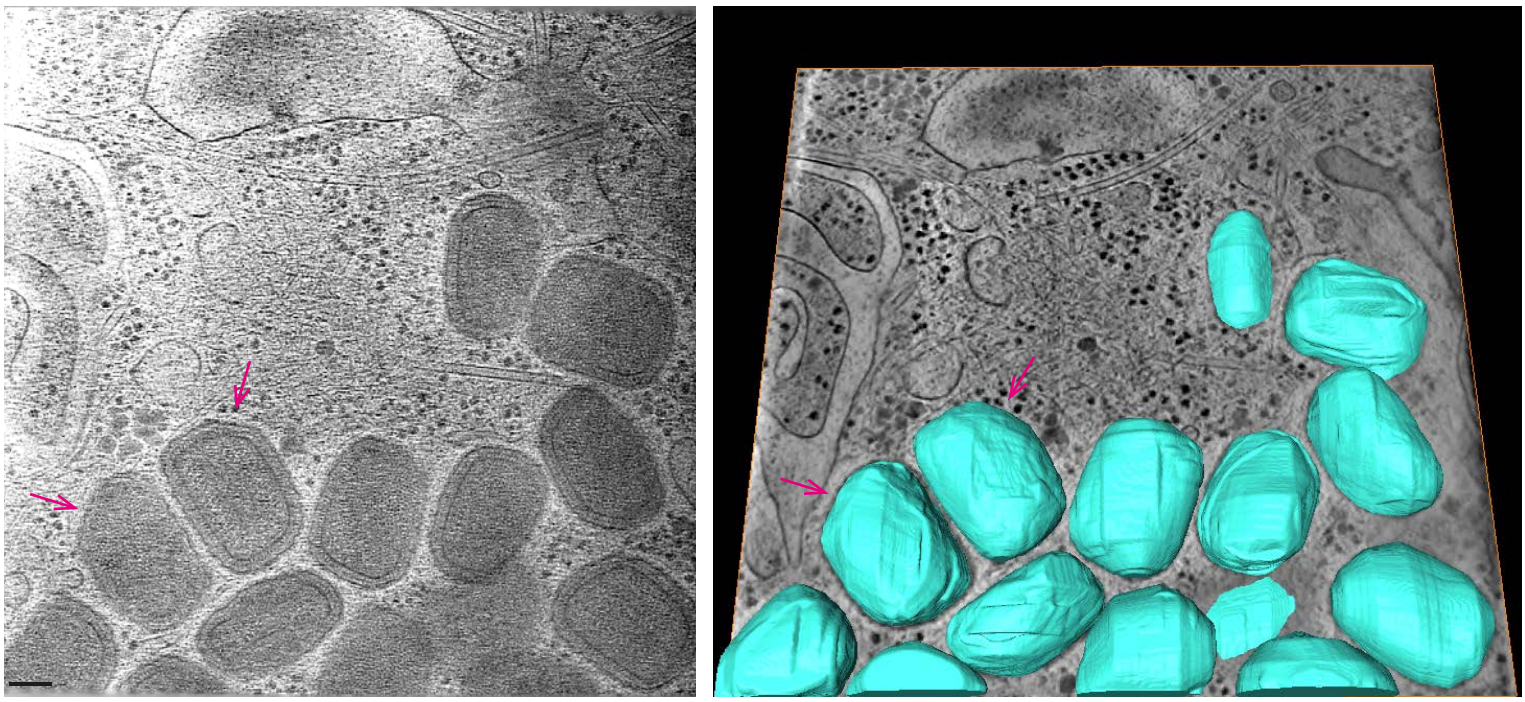

Figure 1

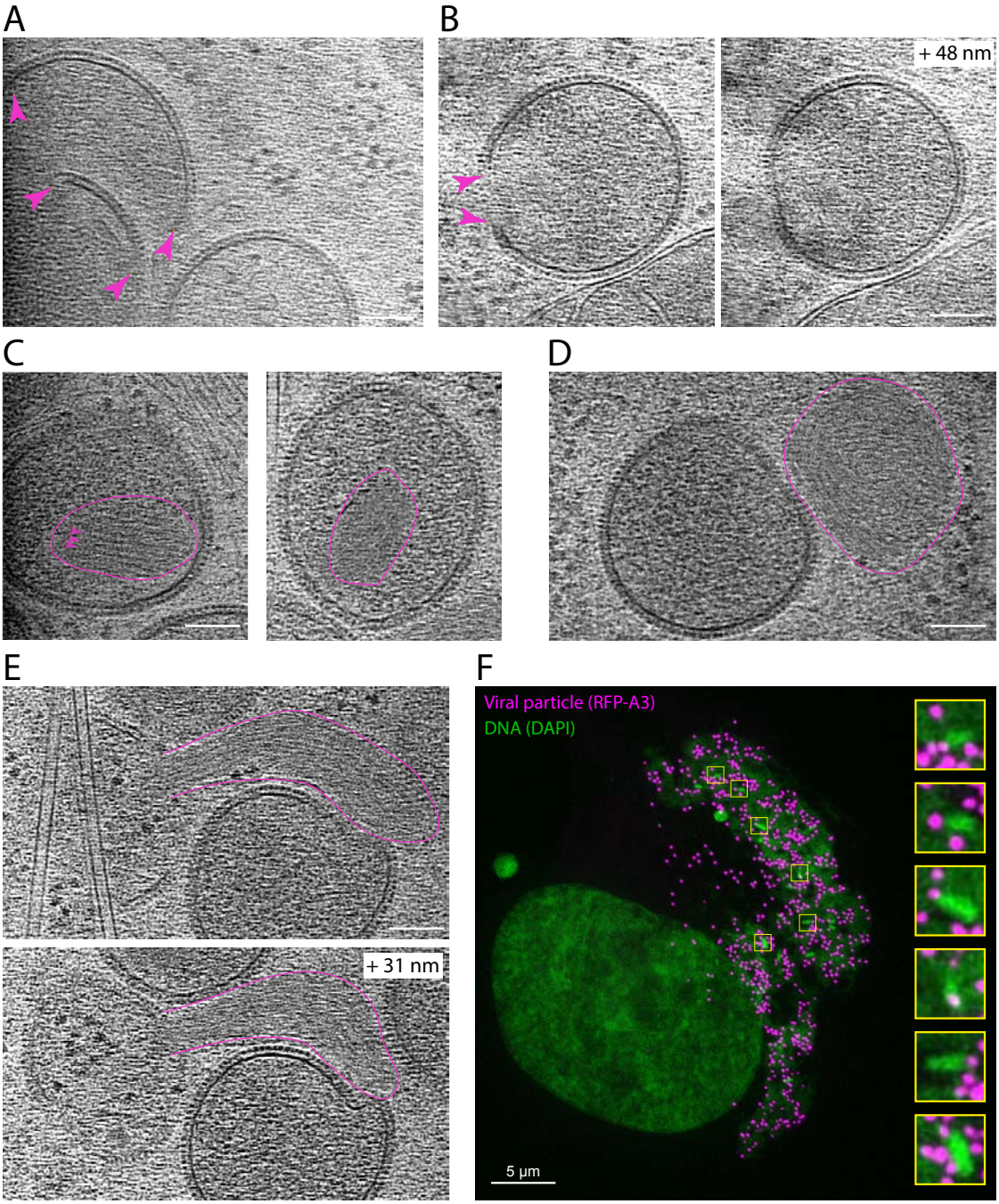

Figure 2

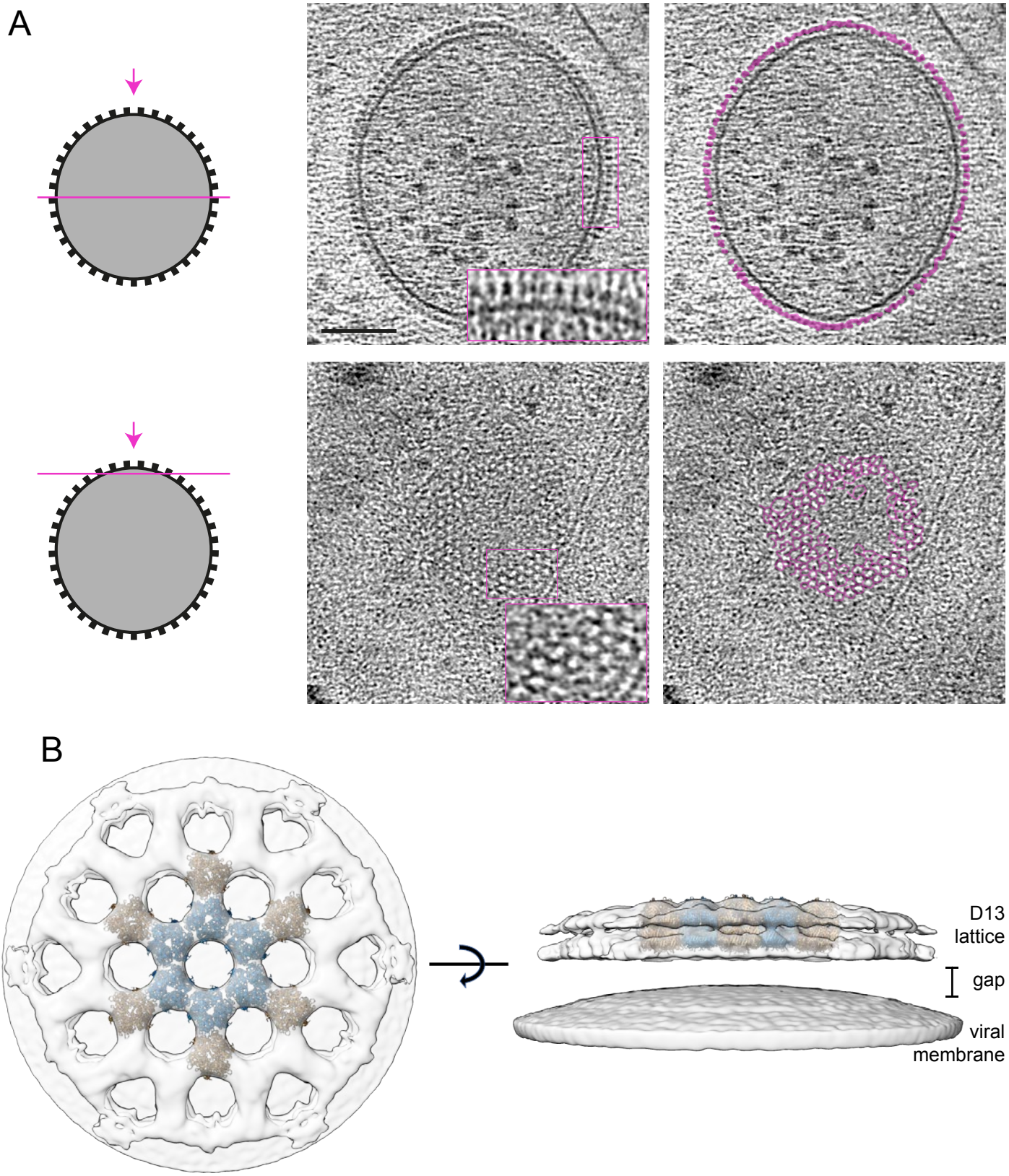

Figure 3

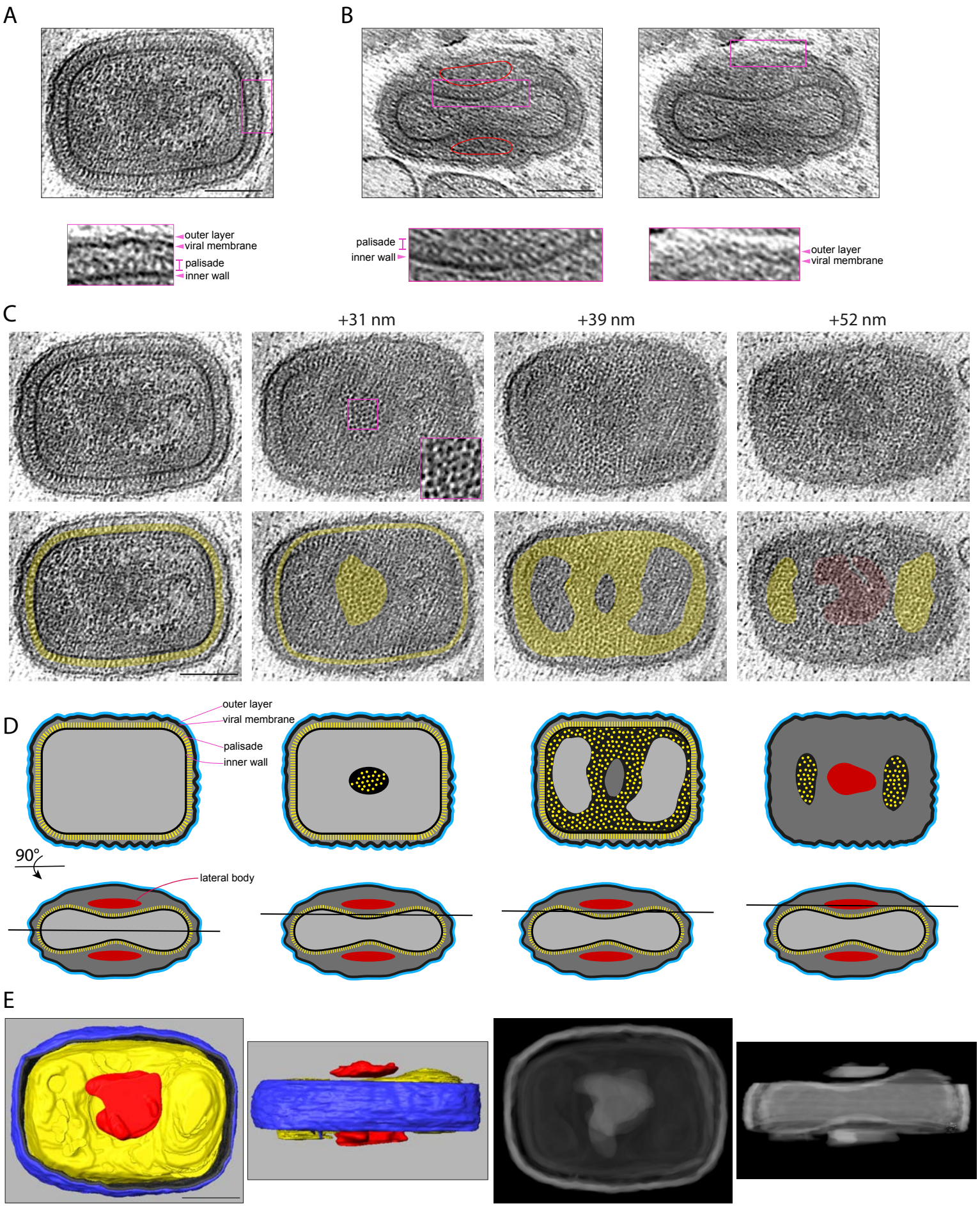
A
B
outer layer
viral membrane
palisade
inner wall
palisade
inner wall
outer layer
viral membrane
C
+31 nm
+39 nm
+52 nm
D
outer layer
viral membrane
palisade
inner wall
90°
lateral body
E

Figure 4

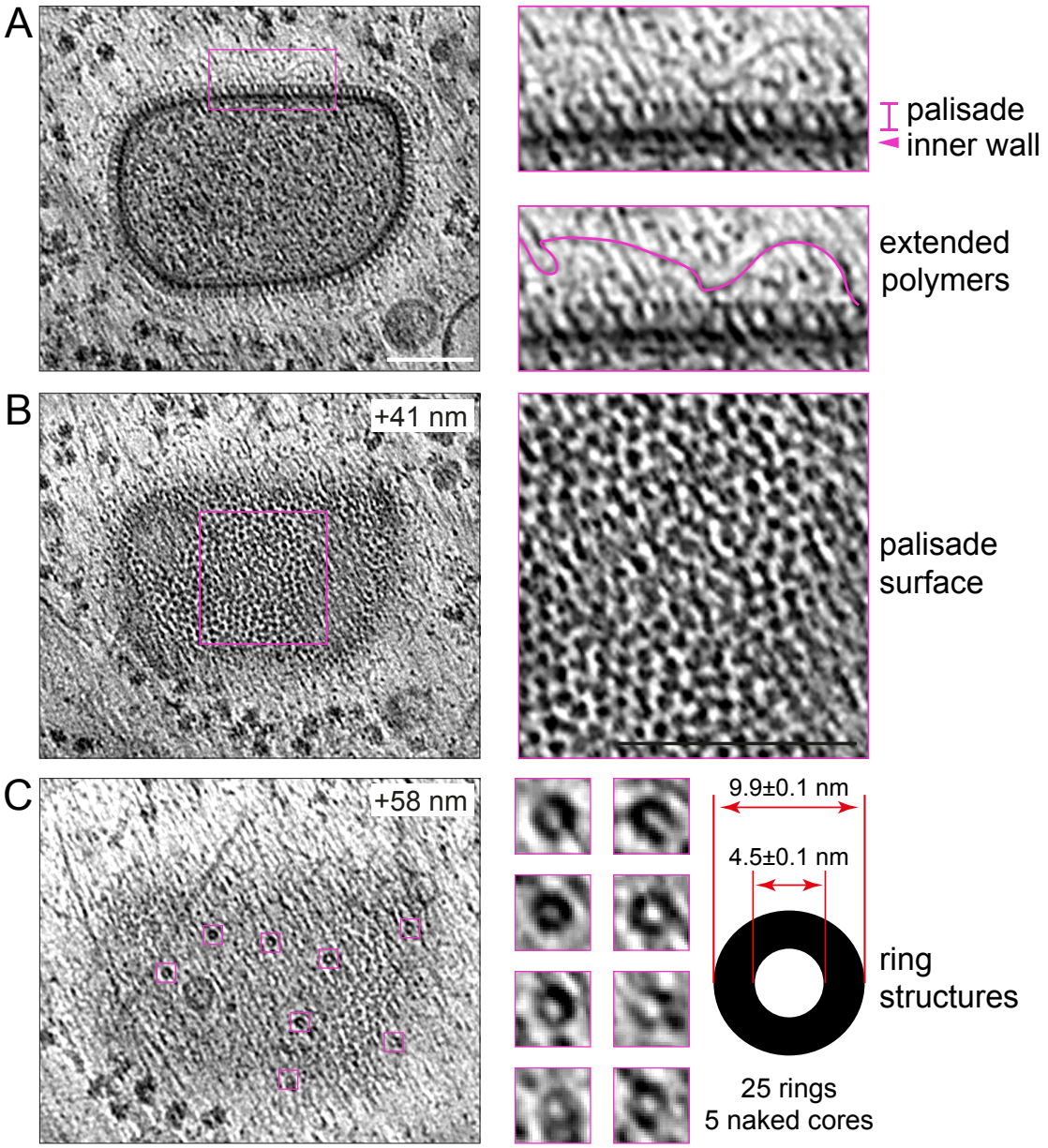
A
palisade
inner wall
extended
polymers
B
+41 nm
palisade
surface
C
+58 nm
9.9±0.1 nm
4.5±0.1 nm
ring
structures
25 rings
5 naked cores

Figure 5

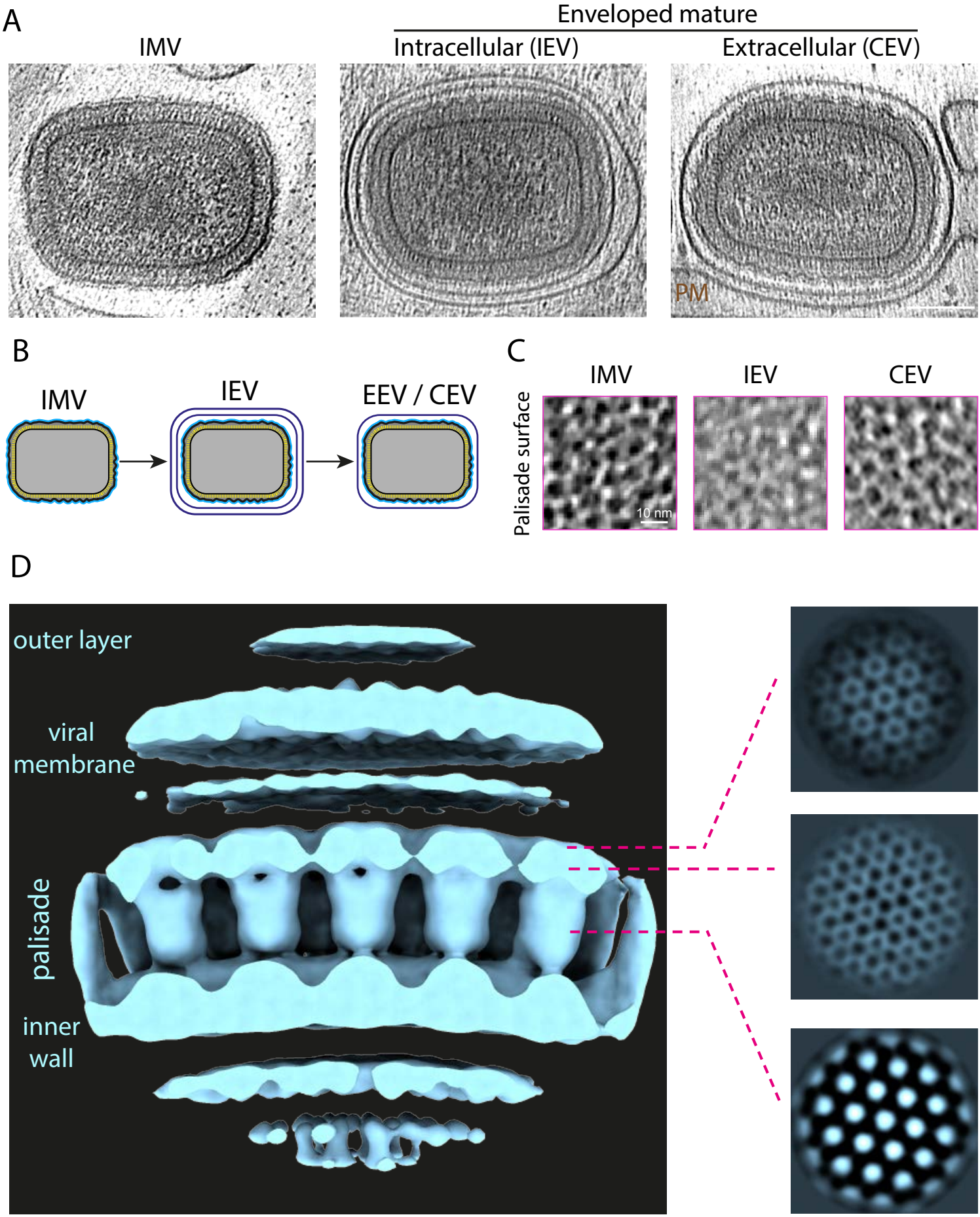
A
Enveloped mature
IMV
Intracellular (IEV)
Extracellular (CEV)
PM
B
IMV
IEV
EEV / CEV
C
IMV
IEV
CEV
Palisade surface
10 nm
D
outer layer
viral membrane
palisade
inner wall

Figure 6

A

	Immature virus (IV)		Intracellular mature virus (IMV)	
Approximate shape	Sphere		Triaxial ellipsoid	
Dimensions (nm)	Diameter	351.89 ± 2.88	Major axis	351.70 ± 3.31
			Intermediate axis	280.53 ± 3.66
			Minor axis*	198.04 ± 4.94
Perimeter (middle plane, (nm)	1106.39 ± 8.58		1087.75 ± 11.25	
Calculated volume (nm^3)	2.28×10^7		1.02×10^7	

B

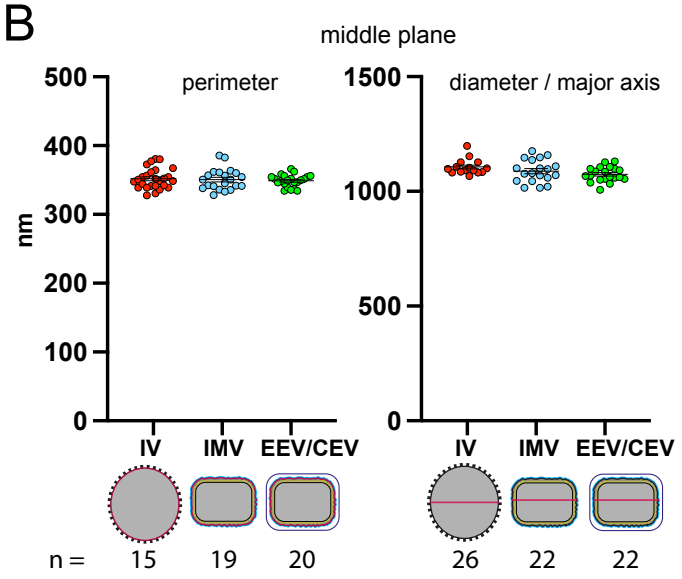

C

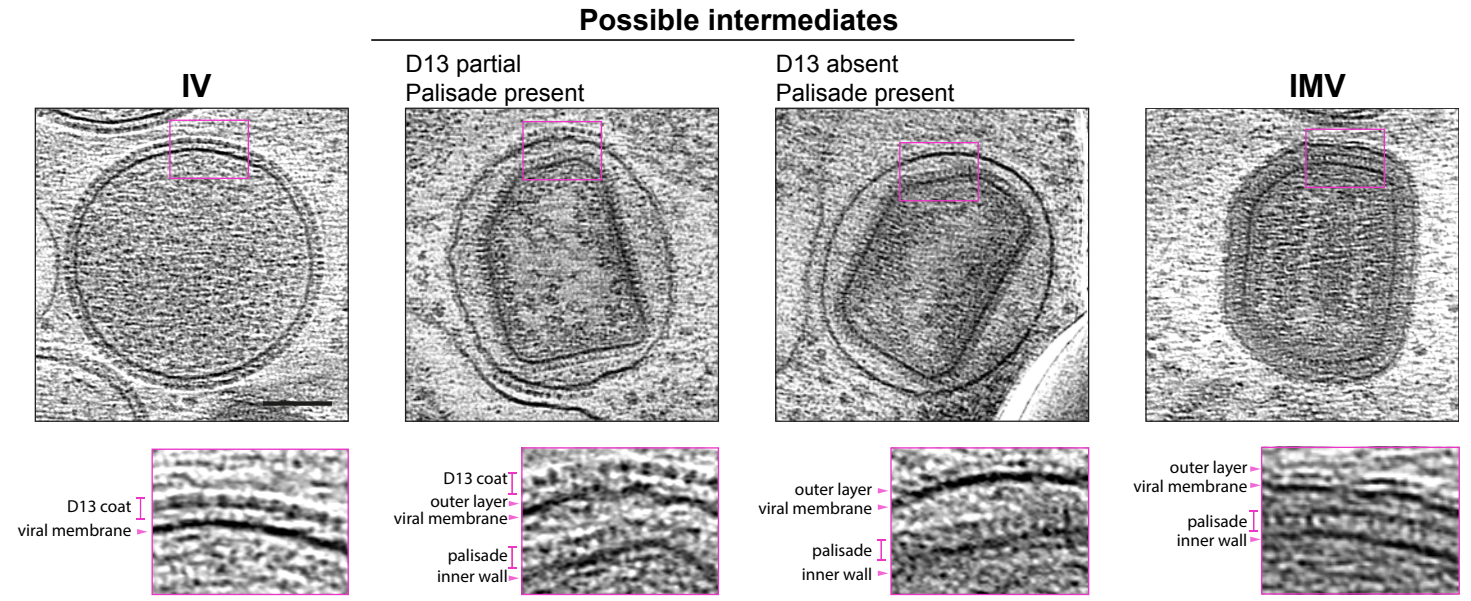

D

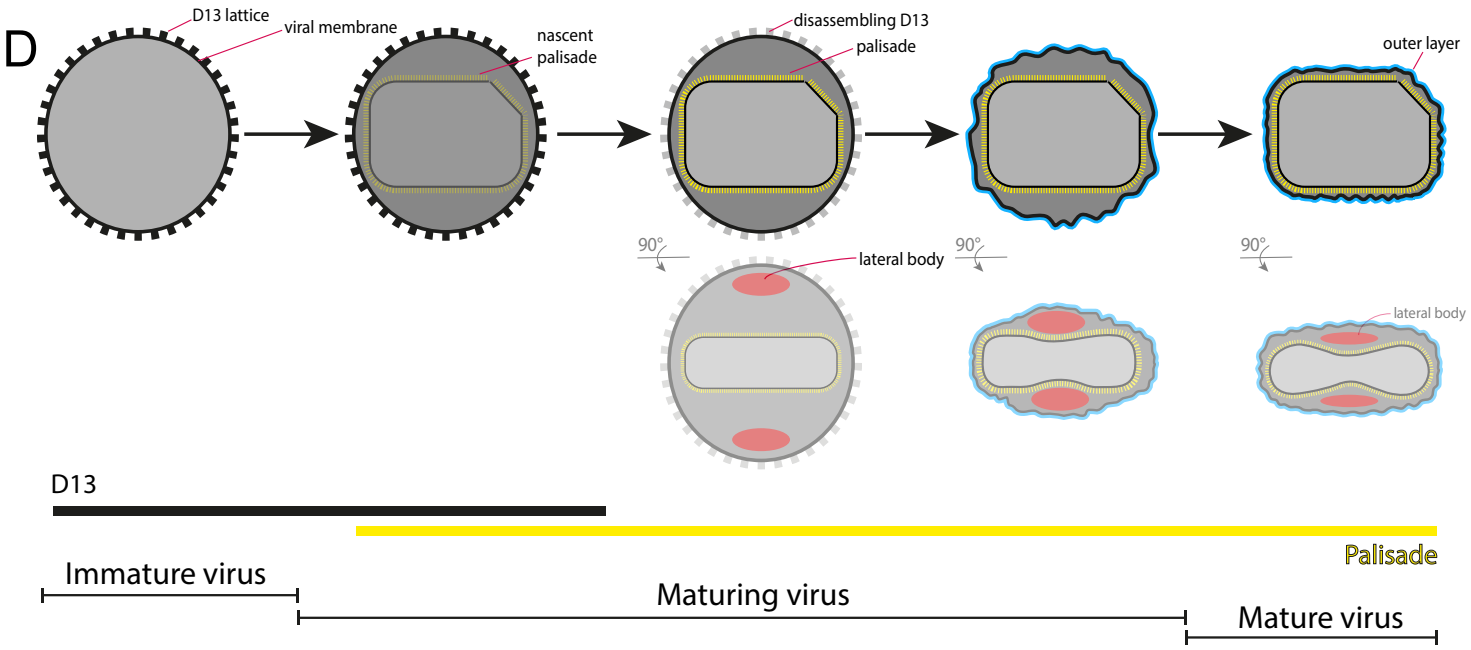

Figure 7

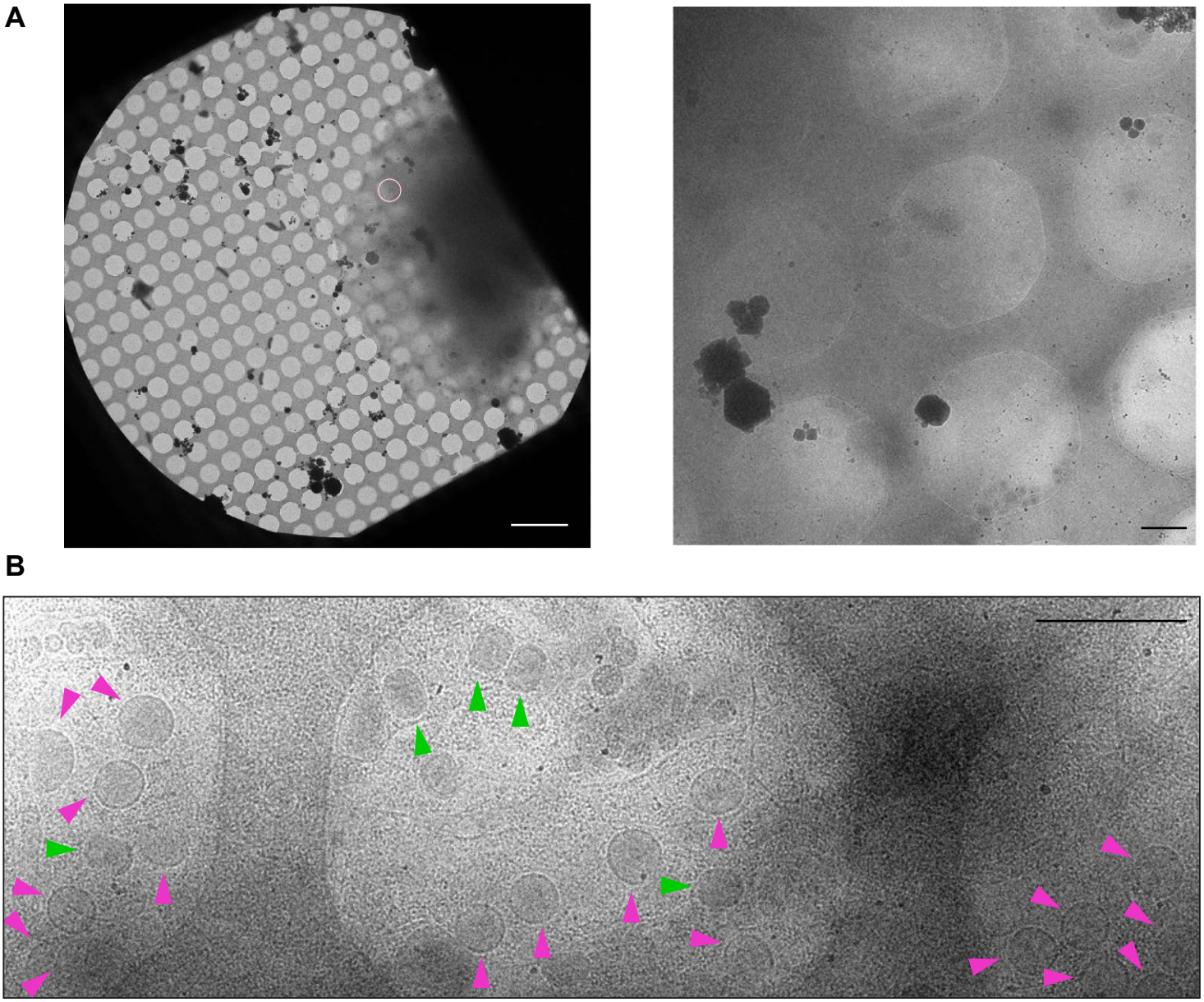

Supplementary Figure 1

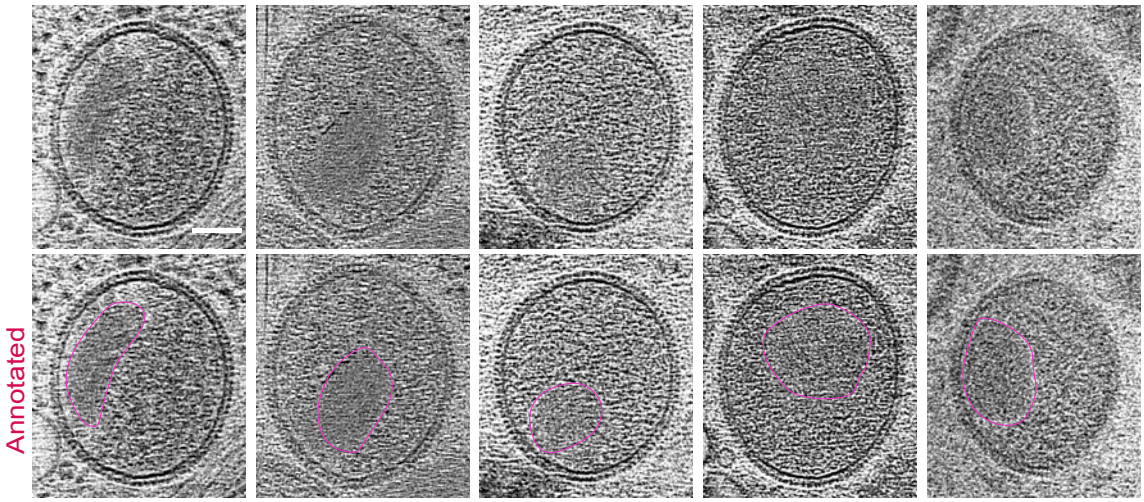

Supplementary Figure 2

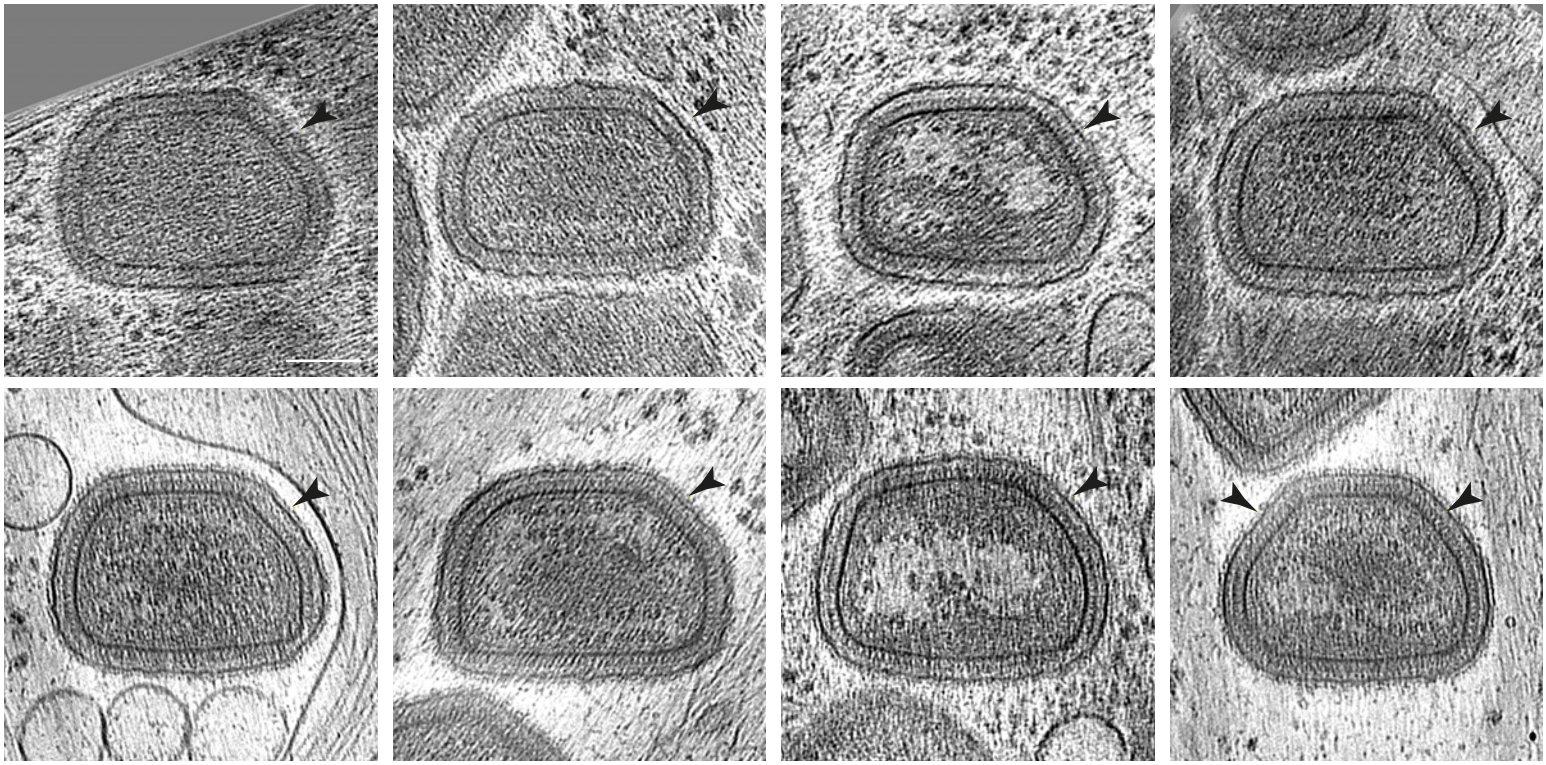

Cut corner : 48.9% No cut corner : 51.1% n = 94 IMV

Supplementary Figure 3

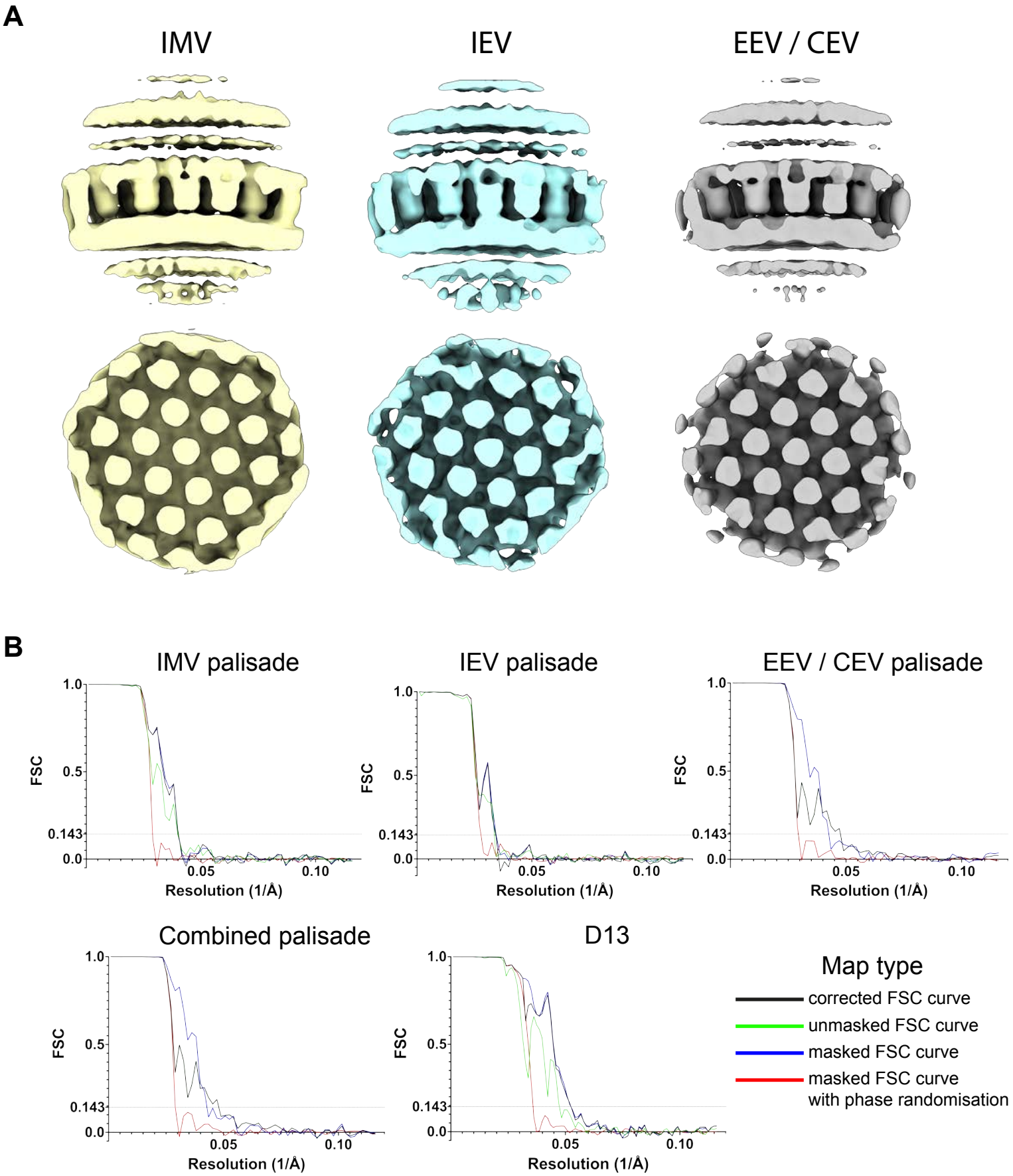

Supplementary Figure 4